International Journal of Modern Physics A (2022) 2241004 (41 pages)
© World Scientific Publishing Company DOI: 10.1142/S0217751X22410044



Quantum corrections to soliton energies

N. Graham

Department of Physics, Middlebury College, Middlebury, VT 05753, USA ngraham@middlebury.edu

H. Weigel*

Institute for Theoretical Physics, Physics Department, Stellenbosch University, Matieland 7602, South Africa weigel@sun.ac.za

> Received 27 January 2022 Accepted 10 February 2022 Published 27 April 2022

We review recent progress in the computation of leading quantum corrections to the energies of classical solitons with topological structure, including multi-soliton models in one space dimension and string configurations in three space dimensions. Taking advantage of analytic continuation techniques to efficiently organize the calculations, we show how quantum corrections affect the stability of solitons in the Shifman–Voloshin model, stabilize charged electroweak strings coupled to a heavy fermion doublet, and bind Nielsen–Olesen vortices at the classical transition between type I and type II superconductors.

Keywords: Soliton; vacuum polarization energy; spectal method.

1. Introduction

The existence of degenerate vacuum configurations in a classical field theory allows for the possibility of topological soliton, or, more precisely, solitary wave solutions, which are solutions to the field equations with localized energy densities. Because such solitons are stabilized by global properties of the classical solution, one expects them to remain stable when quantum effects are included. However, in a variety of situations, quantum corrections can alter the classical results in a significant way. These effects can be formulated as the shift in the zero-point (vacuum) energies of the fluctuations when subjected to the potential induced by the soliton. This

^{*}Corresponding author.

vacuum polarization energy (VPE) is^a

$$\Delta E = \frac{1}{2} \sum_{k} \left(\omega_k - \omega_k^{(0)} \right) + E_{\rm CT}, \tag{1}$$

where ω_k and $\omega_k^{(0)}$ are the energy eigenvalues of the fluctuations in the background of the soliton and the translationally invariant vacuum, respectively, and $E_{\rm CT}$ is the counterterm contribution, described below. The formal sum in Eq. (1) can be expressed as a discrete sum over bound states plus a continuum integral over scattering states. We note that Eq. (1) may also be taken as the starting point for studies of the Casimir force on conductors due to the exchange of virtual photons, ^{2,3} and so the VPE is often also called the Casimir energy. For a charged soliton, one can include effects of occupied levels, but such contributions must always be considered together with the VPE since they appear at the same order in \hbar .

Even when taking the difference of energy levels as in Eq. (1), the sum over zero-point energies diverges, so the theory must be regularized, and counterterm contributions $E_{\rm CT}$ must be added to render the VPE finite. In renormalizable theories, the counterterms are linear combinations of terms already present in the local Lagrangian before quantization. The coefficients of these terms are determined from conditions on Green's functions that do not depend on the field configuration under consideration. These renormalization conditions define masses and couplings in the quantum theory that are fixed from experimental data. Based on these inputs, one then obtains unambiguous predictions from calculations in the renormalized theory.

Particularly because most applications in four space—time dimensions ultimately require numerical analysis, additional tools are required to pass from these formal expressions to tractable calculations with no cancellations of large or cutoff-dependent quantities. Without such tools, early calculations required extremely high precision. As was already recognized in the earliest VPE calculations, scattering theory methods can play an invaluable role in improving this situation. In this approach, the continuum part of the sum in Eq. (1) is rewritten as an integral over the change of the density of states, which in turn is related to the scattering phase shift. The VPE calculation is then connected with standard renormalization procedures by identifying contributions from the Born approximation of the phase shift with the corresponding terms in the Feynman diagram expansion for the VPE.^{7,8}

Even with these tools, however, the sums and integrals over the entire spectrum of quantum fluctuations are still challenging numerically for phenomenologically relevant models. As in other numerical computations in quantum field theory, it is helpful to use contour integration to shift the integral over the density of states to the imaginary momentum axis. One immediate benefit of this approach is that bound states no longer need to be identified explicitly, since their contributions are

^aUnless noted otherwise, we write formulas for boson fluctuations. Fermion fluctuations require an overall minus sign.

exactly canceled by those from poles in the contour integral.⁹ Furthermore, careful extension of the variable phase approach to scattering theory¹⁰ can enable one to replace oscillating functions with decaying exponential functions (while avoiding growing exponential functions),^{8,11} significantly improving the efficiency of the numerical computation.

Owing to its fundamental importance in quantum field theory, there is an extensive literature covering many approaches to and applications of VPE calculations. A necessarily incomplete summary includes Green's function methods, ^{12–15} which allow for a similar Born approximation identification of the divergent diagrams and counterterms; heat kernel techniques, based on the proper-time representation of the determinant, which can be used to provide long-wavelength approximations, ^{16–18} for sufficiently smooth background configurations, as well as exact results, ^{9, 19–23} although the comparison to standard renormalization conditions is more difficult in this approach; the Gel'fand–Yaglom method, ^{24–30} which obtains the energy sum in Eq. (1) from the solution to a differential equation; the world-line formalism, ^{31–34} which uses more extensive numerical computation and as a result can accommodate configurations without sufficient symmetry for a partial wave expansion; and generalized derivative expansion methods, which can yield both exact results when summed to all orders^{35–37} and simpler approximate results for slowly varying backgrounds. ^{38–41}

In this review, we begin in Sec. 2 by recapitulating the spectral methods approach for computing the VPE, with emphasis on the effectiveness of the imaginary momentum integration. We then discuss three situations where quantum corrections can qualitatively affect the properties of classical solitons with topological charge arising from a winding number. In Sec. 3, we summarize how the VPE can destabilize multi-soliton solutions in one space dimension. In Sec. 4, we show how coupling to a heavy fermion can stabilize electroweak strings by allowing the energy of fermions bound to the string to be lower than that of the same number of free fermions. Finally, in Sec. 5, we discuss quantum corrections to Nielsen–Olesen vortices as a function of winding number, and show that in the BPS case of equal gauge and Higgs masses, quantum corrections favor higher winding over a corresponding number of isolated vortices with unit winding, while in the classical model these energies are equal.

2. Spectral Methods

Spectral methods are the main tool to compute the VPE of static, extended field configurations. These configurations induce a potential for small amplitude fluctuations, which are treated by standard techniques of scattering theory in quantum mechanics. They provide the bound state energies, ω_j , which directly enter the VPE, as well as the phase shifts $\delta(k)$ (or more generally the scattering matrix) as a function of the wave-number k for single-particle energies above threshold given by the mass m of the fluctuating field. Those phase shifts parameterize the change

in the density of continuum modes via the Friedel-Krein formula⁴²

$$\Delta \rho_{\ell} = \frac{1}{\pi} \frac{d\delta_{\ell}(k)}{dk},\tag{2}$$

where we assume that the scattering potential has sufficient symmetry to allow a partial wave expansion, represented by the ℓ index.

In turn, that change determines the continuum contribution to the VPE

$$\Delta E = \frac{1}{2} \sum_{j}^{\text{b.s.}} \omega_{j} + \frac{1}{2} \int_{0}^{\infty} dk \sum_{\ell} \sqrt{k^{2} + m^{2}} \, \Delta \rho_{\ell} + E_{\text{CT}}$$

$$= \frac{1}{2} \sum_{j}^{\text{b.s.}} \omega_{j} + \int_{0}^{\infty} \frac{dk}{2\pi} \sum_{\ell} \sqrt{k^{2} + m^{2}} \, \frac{d\delta_{\ell}(k)}{dk} + E_{\text{CT}}.$$
(3)

Here the partial wave sum includes any associated degeneracy factors, e.g. $2\ell + 1$ for angular momentum in three space dimensions.

Eventually the analytic properties of scattering data allow for a more efficient computation of the VPE by introducing imaginary momenta k = it with $t \ge 0$. Details of that approach have been reviewed elsewhere,⁸ so here we will focus on the main features for completeness.

2.1. Scattering data

To compute the scattering data that enter Eq. (3), we first write down the Schrödinger type equation for the radial part of the fluctuation wave functions

$$\psi_{\ell,k}''(x) = -k^2 \psi_{\ell,k}(x) + \frac{1}{x^2} L^2 \psi_{\ell,k}(x) + \sigma(x) \psi_{\ell,k}(x), \tag{4}$$

where a prime indicates the derivative with respect to the radial coordinate x and L^2 is square of the angular momentum eigenvalue. In one space dimension x is position on the real axis with $L^2=0$, while in three dimensions $x\geq 0$ and $L^2=\ell(\ell+1)$, for example. If the induced potential $\sigma(x)$ is attractive, there are discrete bound state solutions with $\int dx |\psi_k(x)|^2 \leq \infty$ and energy eigenvalues $\omega_j = \sqrt{m^2 - \kappa_j^2}$ for $k^2 = -\kappa_j^2 < 0$. In general we consider a multi-channel problem, so that $\sigma(x)$ is matrix valued while $\psi_{\ell,k}(x)$ is an array of n wave functions, where n is the number of channels. We can then define an $n \times n$ matrix $\Psi_{\ell,k}(x)$, whose different columns represent independent boundary conditions. In particular, introducing $\mathcal{H}_{\ell,k}(x)$ as the diagonal matrix containing the free outgoing solutions, we parameterize $\Psi_{\ell,k}(x) = \mathcal{F}_{\ell,k}(x) \cdot \mathcal{H}_{\ell,k}(x)$ and obtain the wave-equation

$$\mathcal{F}_{\ell,k}^{"}(x) = -2k\mathcal{F}_{\ell,k}(x)' \cdot \mathcal{H}_{\ell,k}^{"}(x) \cdot \mathcal{H}_{\ell,k}^{-1}(x) + \sigma(x) \cdot \mathcal{F}_{\ell,k}(x). \tag{5}$$

Imposing the boundary condition $\lim_{x\to\infty} \mathcal{F} = 1$ and observing that the original wave-equation (4) is real, we get the physical scattering solution as the combination

$$\Psi_{\ell,k}^{(\mathrm{sc})}(x) = \mathcal{F}_{\ell,k}^*(x) \cdot \mathcal{H}_{\ell,k}^*(x) - \mathcal{F}_{\ell,k}(x) \cdot \mathcal{H}_{\ell,k}(x) \cdot \mathcal{S}(k), \tag{6}$$

since $\mathcal{H}_{\ell,k}^*(x)$ asymptotically describes incoming waves. The scattering matrix, \mathcal{S} , is extracted from the regularity condition^b $\lim_{x\to 0} \Psi_{\ell,k}^{(\mathrm{sc})}(x) = 0$. Finally, the phase shift entering Eq. (3) is

$$\delta_{\ell}(k) = \frac{1}{2i} \ln[\det S_{\ell}(k)] = \frac{1}{2i} \ln \lim_{x \to 0} [\det(\mathcal{F}_{\ell,k}^{*}(x)\mathcal{F}_{\ell,k}^{-1}(x))]. \tag{7}$$

2.2. Renormalization

So far, our expression for the VPE has been quite formal since in Eq. (3) we still have to combine the infinities in the momentum integral and the counterterms to obtain a finite result. Conventionally the counterterm coefficients are determined from the perturbative expansion of Green's functions via the computation of Feynman diagrams. We can incorporate that scheme by first noting that there is a Feynman diagram expansion for the quantum action in the presence of the potential $\sigma(x)$. The leading quantum correction is the sum of all one-loop diagrams

$$\operatorname{Tr} \ln \left[\frac{D_2 + \sigma(x)}{D_2} \right] = - + - + - + - + \cdots, \quad (8)$$

where D_2 denotes the (covariant) second-order differential operator associated with the free wave-equation. The double lines represent insertions of the Fourier transform of $\sigma(x)$, so that the Feynman diagrams are given as integrals over those Fourier momenta and the loop momentum. Dividing by D_2 on the left-hand side represents the subtraction of $\omega_k^{(0)}$ in Eq. (1). Since the potential is static, the energy is just the negative action per unit time. Hence it is straightforward to associate the energy $E_{\rm FD}^{(n)}$ with the Feynman diagrams containing n insertions of $\sigma(x)$.

On the other hand, we can expand the Jost solutions according to increasing orders in the potential by writing $\mathcal{F} = \mathbb{1} + \mathcal{F}^{(1)} + \mathcal{F}^{(2)} + \cdots$ (omitting labels for brevity). The $\mathcal{F}^{(n)}$ are subject to the differential equations¹⁰

$$\mathcal{F}^{(1)\prime\prime} = -2\mathcal{F}^{(1)\prime} \cdot \mathcal{H}' \cdot \mathcal{H}^{-1} + \sigma, \quad \mathcal{F}^{(2)\prime\prime} = -2\mathcal{F}^{(2)\prime} \cdot \mathcal{H}' \cdot \mathcal{H}^{-1} + \sigma \mathcal{F}^{(1)}, \dots,$$
(9)

with boundary conditions $\lim_{x\to\infty} \mathcal{F}^{(n)}(x) = 0$. In turn this Born expansion yields the n^{th} order contribution to the phase shift $\delta_{\ell}^{(n)}(k)$ by collecting terms of order n in Eq. (7). Using Eq. (3), each order can be associated with an energy computed from scattering data. Hence we have two expansions with respect to the same quantity. They are equal order by order and we can write

$$\Delta E = \frac{1}{2} \sum_{j=1}^{\text{b.s.}} \omega_j + \int_0^\infty \frac{dk}{2\pi} \sum_{\ell} \sqrt{k^2 + m^2} \left[\frac{d\delta_{\ell}(k)}{dk} \right]_N + \sum_{n=1}^N E_{\text{FD}}^{(n)} + E_{\text{CT}}, \quad (10)$$

^bThe symmetric channel is one space dimension has $\lim_{x\to 0} \Psi'^{(\text{sc})}_{\ell,k}(x) = 0$ and a positive relative sign in Eq. (6).

where the subscript indicates that the first N terms of the expansions are subtracted: $[\delta_{\ell}(k)]_N = \delta_{\ell}(k) - \sum_{n=1}^N \delta_{\ell}^{(n)}(k)$. Integrating by parts and using Levinson's theorem⁴³ yields the VPE in terms of binding energies as

$$\Delta E = \frac{1}{2} \sum_{j}^{\text{b.s.}} (\omega_j - m) - \int_0^\infty \frac{dk}{2\pi} \sum_{\ell} \frac{k}{\sqrt{k^2 + m^2}} [\delta_{\ell}(k)]_N + \sum_{n=1}^N (E_{\text{FD}}^{(n)} + E_{\text{CT}}).$$
(11)

The power of this expression is that it is a combination of finite terms. The momentum integral has become finite because sufficiently many $\delta_{\ell}^{(n)}(k)$ are subtracted from the exact phase shift. The Feynman diagram and counterterm energies are computed with a common regularization scheme such that the regulator disappears. Eventually we will use dimensional regularization with on-shell renormalization conditions; i.e. poles and residues of propagators do not have quantum corrections. These conditions are augmented by the "no-tadpole" condition that quantum corrections to the vacuum expectation values of the fields vanish.

We stress that for the formalism to be valid, the convergence of the expansion in Eq. (8) is not necessary because we only consider a finite number of terms. It is also important to stress that, though the Born series features prominently in the approach, the phase shifts are not obtained by any kind of approximation.

We have obtained Eq. (11) by relating the change in the density of states to the phase shift. The quantum field theory derivation that integrates the vacuum expectation value of the energy density can be found in Ref. 11.

2.3. Imaginary momenta

It will be helpful in our calculations to make use of the analytic properties of scattering data. Note that $\mathcal{F}_{\ell,k}(x) \cdot \mathcal{H}_{\ell,k}(x)$ is the Jost solution to the scattering problem, while $F_{\ell}(k) = \lim_{x\to 0} \det \mathcal{F}_{\ell,k}(x)$ is the Jost function, which is analytic for $\operatorname{Im}(k) \geq 0$. For the definition in terms of outgoing waves, the elements of $\mathcal{H}_{\ell,k}(x)$ are Hankel functions with asymptotic behavior proportional to e^{ikx} . It is therefore clear that $\mathcal{F}_{-k}(x) = \mathcal{F}_k^*(x)$ for real k. We then observe that the phase shift

$$\delta_{\ell}(k) = \frac{i}{2} (\ln F_{\ell}(k) - \ln F_{\ell}(-k))$$
(12)

is an odd function of k. We thus write

$$\int_0^\infty \frac{dk}{2\pi} \sum_{\ell} \sqrt{k^2 + m^2} \left[\frac{d\delta_{\ell}(k)}{dk} \right]_N = \frac{i}{2} \int_{-\infty}^\infty \frac{dk}{2\pi} \sum_{\ell} \sqrt{k^2 + m^2} \left[\frac{d\ln F_{\ell}(k)}{dk} \right]_N.$$
(13)

To evaluate the right-hand side by analytic continuation and contour integration, we recall that

• with the subtraction of the Born terms, there is no contribution from the semicircles at $|k| \to \infty$; • the Jost function has simple zeros at the bound state wave numbers while the Born terms have no zeros (otherwise bound states would be perturbative effects):

$$\left[\frac{d\ln F_{\ell}(k)}{dk}\right]_{N} = \frac{1}{k - \mathrm{i}\kappa_{j}} + \cdots \quad \text{for } k \approx \mathrm{i}\kappa_{j};$$

• the square root induces a branch cut along the imaginary axis k = it:

$$\sqrt{(it+\epsilon)^2 + m^2} - \sqrt{(it-\epsilon)^2 + m^2} = 2i\sqrt{t^2 - m^2}$$

for $t \ge m$ and $\epsilon \to 0^+$.

Collecting pieces we have

$$\int_0^\infty \frac{dk}{2\pi} \sum_{\ell} \sqrt{k^2 + m^2} \left[\frac{d\delta_{\ell}(k)}{dk} \right]_N$$

$$= -\frac{1}{2} \sum_{i}^{\text{b.s.}} \sqrt{m^2 - \kappa_j^2} - \int_m^\infty \frac{dt}{2\pi} \sum_{\ell} \sqrt{t^2 - m^2} \left[\frac{d \ln F_{\ell}(it)}{dt} \right]_N, \quad (14)$$

where the sum on the right-hand side cancels the explicit bound state contribution in Eq. (10).⁹ Again integrating by parts yields for the VPE

$$\Delta E = \int_{m}^{\infty} \frac{dt}{2\pi} \sum_{\ell} \frac{t}{\sqrt{t^2 - m^2}} [\nu_{\ell}(t)]_N + \sum_{n=1}^{N} E_{\text{FD}}^{(n)} + E_{\text{CT}},$$
 (15)

where $\nu_{\ell}(t) = \ln F_{\ell}(it) = \lim_{x\to 0} \ln \det \mathcal{F}_{\ell,it}(x)$. We obtain $\mathcal{F}_{\ell,it}(x)$ and its Born expansion by integrating Eqs. (5) and (9) with $\mathcal{H}_{\ell,k}(x) \to \mathcal{H}_{\ell,it}(x)$. It is worth noting that $\det \mathcal{F}_{\ell,it}(x)$ is a real quantity.

In certain cases the limit $x \to 0$ needs specific treatment. In two space dimensions, the regular solution approaches a constant while the irregular one diverges logarithmically in the zero angular momentum channel. Numerically these solutions are cumbersome to disentangle and it is not sufficient simply to read off $\mathcal{F}_{\ell,it}(x)$ at some very small x; rather a sophisticated extrapolation is required. Furthermore singular background potentials may require additional subtractions because the Born expansion reflects that singularity, for example in the case of vortices in scalar electrodynamics. Also, fermion masses explicitly enter the spinor wave functions and the effective masses at spatial infinity and $x \to 0$ may differ. This effect must be incorporated when extracting $\nu(t)$ from $\mathcal{F}_{\ell,it}(x)$ as well. We will return to these issues in Secs. 4 and 5.

2.4. Interface configurations

A problem that often arises in contexts such as the Casimir force¹¹ is that of computing the VPE originating from (idealized) boundary conditions of infinitely large plates. In such a problem, the plate acts like a domain wall, with translational invariance along a plane, while there is a localized structure in the orthogonal dimension. Similarly, strings stretch along an axis with translational invariance

while having a soliton-like configuration in the plane orthogonal to that axis. The scattering problem in the translationally invariant subspace is trivial, which introduces subtleties in the computation of the VPE and in particular its regularization and renormalization.

We consider a general scenario with a localized (classical) configuration contained in the n-dimensional subspace \mathbb{R}^n . It is embedded in a higher-dimensional space such that there is translational invariance in an m-dimensional subspace \mathbb{R}^m . The combined fluctuation wave function is then

$$\varphi(\boldsymbol{x}, \boldsymbol{y}) = e^{i\boldsymbol{p}\cdot\boldsymbol{y}} \,\tilde{\varphi}(\boldsymbol{x}),\tag{16}$$

where $\mathbf{p} \in \mathbb{R}^m$ is the transverse momentum conjugate to the extra dimensions \mathbf{y} . The reduced wave function $\widetilde{\varphi}(\mathbf{x})$ is subject to a wave-equation in n spatial dimensions with a background potential $\sigma(x)$ similar to Eq. (4). Then the dispersion relations for the scattering and bound states of the (n+m)-dimensional problem are $(p=|\mathbf{p}|$ and $k=|\mathbf{k}|)$

$$\omega(k,p) = \sqrt{m^2 + k^2 + p^2} \quad \text{and} \quad \omega_j(p) = \sqrt{m^2 + p^2 - \kappa_j^2},$$

respectively. Here, k and κ_j are the (imaginary) momenta conjugate to $\boldsymbol{x} \in \mathbb{R}^n$. We get the corresponding densities of states by simply multiplying the free density of states of the m-dimensional transverse space

$$\rho_{\ell}(\boldsymbol{p}, k) = \frac{1}{\pi} \frac{d\delta_{\ell}(k)}{dk} \frac{V_m}{(2\pi)^m} \quad \text{and} \quad \rho_{j}(\boldsymbol{p}) = \frac{V_m}{(2\pi)^m}.$$
 (17)

This in turn yields the VPE per unit transverse volume

$$\mathsf{E}_{m,n} = \frac{\Delta E}{V_m} = \int \frac{d^m p}{(2\pi)^m} \left[\int_0^\infty \frac{dk}{2\pi} \sum_{\ell} (\omega(k,p) - \mu(p)) \frac{d\delta_{\ell}(k)}{dk} + \frac{1}{2} \sum_{j} (\omega_j(p) - \mu(p)) \right] + \frac{E_{\mathrm{CT}}}{V_m}, \tag{18}$$

where the mass coefficient $\mu(p)=\sqrt{m^2+p^2}$ must be taken to depend on the transverse momentum. In this form the subtlety mentioned above emerges immediately: The p integral is divergent but the phase shift does not involve p and thus there is no Born subtraction that can render this integral finite. To see this more clearly, we integrate over p in dimensional regularization:

$$\mathsf{E}_{m,n} = -\frac{\Gamma(-\frac{1+m}{2})}{2(4\pi)^{\frac{m+1}{2}}} \left[\int_0^\infty \frac{dk}{\pi} \sum_{\ell} (\omega^{m+1}(k,0) - m^{m+1}) \frac{d}{dk} [\delta_{\ell}(k)]_N + \sum_{j} (\omega_j(0)^{m+1} - m^{m+1}) \right] + \frac{E_{\mathrm{FD}}^{(N)}}{V_m} + \frac{E_{\mathrm{CT}}}{V_m}, \tag{19}$$

where we have subtracted N Born terms from the phase shift and added them back as the Feynman diagrams $E_{\rm FD}^{(N)}$. Regardless of the number of subtractions, the coefficient produces a divergence for any odd integer m. Let us specifically consider the case m=1, which applies to string configurations. Then the expression in square brackets simplifies to

$$\int_0^\infty \frac{dk}{\pi} k^2 \frac{d}{dk} [\delta_\ell(k)]_N - \sum_j \kappa_j^2 = \int_0^\infty \frac{dk}{\pi} \omega^2(k) \frac{d}{dk} [\delta_\ell(k)]_N + \sum_j \omega_j^2,$$

where the energies refer to those in the *n*-dimensional subspace. The equality above is a consequence of Levinson's theorem. More importantly, this combination vanishes by one of the sum rules that generalize that theorem. ⁴⁶ Hence the residue of the pole from $\Gamma(-\frac{1+m}{2})$ is zero and we can analytically continue to m=1

$$\mathsf{E}_{1,n} = \frac{-1}{8\pi} \left[\int_0^\infty \frac{dk}{\pi} \sum_{\ell} \omega^2(k) \ln \frac{\omega^2(k)}{\overline{\mu}^2} \frac{d}{dk} [\delta_{\ell}(k)]_N + \sum_j \omega_j^2 \ln \frac{\omega_j^2}{\overline{\mu}^2} \right] + \frac{E_{\mathrm{FD}}^{(N)}}{V_m} + \frac{E_{\mathrm{CT}}}{V_m}. \tag{20}$$

The arbitrary energy scale $\overline{\mu}$ has been introduced for dimensional reasons. It has no effect by the sum rule mentioned above. Making use of the relation between the phase shift and the Jost function and its analytic properties allows us to write the integral for imaginary momenta as in Subsec. 2.3. While the bound states energies will no longer appear explicitly, we pick up a contribution from the discontinuity of the logarithm and integrate by parts:

$$\mathsf{E}_{1,n} = \int_{m}^{\infty} \frac{dt}{4\pi} t[\nu(t)]_{N} + \frac{E_{\mathrm{FD}}^{(N)}}{V_{m}} + \frac{E_{\mathrm{CT}}}{V_{m}},\tag{21}$$

where $\nu(t) = \sum_{\ell} \nu_{\ell}(t)$ is the channel sum of the logarithms of the partial wave Jost functions in the *n* dimensions that contain the soliton.

2.5. Fake boson subtraction

In many cases the logarithmically divergent Feynman diagrams are cumbersome to compute. An example is the fermion loop in D=3+1 dimensions, which requires considering diagrams with up to four insertions of the background potential. It is thus desirable to have available a simpler treatment of the logarithmic divergences. The key observation is that the sole purpose of introducing the Born terms and the equivalent Feynman diagrams is to move the ultraviolet divergences out of the momentum integral and combine them with the counterterms, $E_{\rm CT}$. Hence we can use any other subtraction under the momentum integral that can be combined with the same counterterms, $E_{\rm CT}$. In dimensional regularization, $D=3+1\rightarrow 4-2\epsilon$, the logarithmic divergence emerges as $\frac{C_L}{32\pi^2\epsilon}$ where C_L is a local integral over (powers of) the potential in the wave equation. We also note that the Feynman diagram with a scalar loop and two insertions of a potential $V_{\rm B}$ leads to a logarithmic

divergence in $E_{\rm FD}^{(2)}$. This divergence is proportional to the spatial integral of $V_{\rm B}^2$. In this boson theory we can compute $\nu_{\rm B}^{(2)}(t)$, the channel sum of the second-order (in $V_{\rm B}$) contribution to the (summed) logarithm of the Jost function. Next, we take $\overline{\nu(t)}$ to be the logarithm of the Jost function in the original theory with all Born terms removed that lead to divergences higher than logarithmic. This also subtracts the underlying logarithmic divergences in the corresponding Feynman diagrams, so we only need to consider Feynman diagrams that have superficial logarithmic divergences. We add back these subtractions as Feynman diagrams and combine them with the counterterms to $E_{\rm CT}$. We then consider

$$\int_{m}^{\infty} \frac{dt}{2\pi} \frac{t}{\sqrt{t^2 - m^2}} \left[\overline{\nu(t)} - C_{\rm B} \nu_{\rm B}^{(2)}(t) \right] + \overline{E_{\rm FD}} + C_{\rm B} E_{\rm FD}^{(2)} + E_{\rm CT}, \tag{22}$$

where $\overline{E_{\rm FD}}$ are the Feynman diagrams compensating the subtractions in $\overline{\nu(t)}$. Setting $C_{\rm B} = \frac{C_L}{\int d^3 x \, V_{\rm B}^2}$ moves the logarithmic divergence from the momentum integral to the Feynman diagram such that $\overline{E_{\rm FD}} + C_{\rm B} E_{\rm FD}^{(2)} + E_{\rm CT}$ is finite.

As a corollary to this prescription we can consider the finite differences between second-order terms in boson theories with different potentials V_1 and V_2 that are related by the integrals $\int d^3x \, V_1^2 = \int d^3x \, V_2^2$. They have second-order phase shifts $\delta_{\ell,1}^{(2)}(k)$ and $\delta_{\ell,2}^{(2)}(k)$, respectively. The procedure in Eq. (22) implies the relation (with no discrete contributions since Born terms do not account for the nonperturbative bound states),

$$-\int_0^\infty \frac{dk}{2\pi} \sum_{\ell} \frac{k}{\sqrt{k^2 + m^2}} \left[\delta_{\ell,1}^{(2)}(k) - \delta_{\ell,2}^{(2)}(k) \right] = E_{\text{FD},1} - E_{\text{FD},2},$$

which has been numerically verified for particular examples.⁴⁷

Finally, we note that this simple *fake boson* subtraction does not work for quadratic divergences, because then the underlying logarithmic divergences must also be accounted for.

3. Applications in One Space Dimension

In this section, we demonstrate the effectiveness of the imaginary momentum formulation by computing the VPE of sine-Gordon and kink solitons. We also summarize some recent computations of the VPEs for other solitons in one dimension.

3.1. Exactly solvable examples

In Subsec. 2.3, we have emphasized the convenience of the imaginary momentum formalism. Let us briefly demonstrate this in the case of the sine-Gordon and ϕ^4 kink solitons, for which the typical textbook calculations of the VPE are carried out using real momenta.^{1,8} First, we note that for boson theories there is only one

divergent Feynman diagram in D=1+1, which is the tadpole with a single insertion of the background potential (first diagram in Eq. (8)). This diagram can be fully canceled by a counterterm such that $E_{\rm FD}^{(1)}+E_{\rm CT}=0$. Accordingly we only have a single Born subtraction under the momentum integral. The background potentials are of the Pöschl–Teller form⁴⁸

$$\sigma_n(x) = -\frac{n+1}{n} \frac{M^2}{\cosh^2(\frac{Mx}{n})}$$
(23)

with n=1 and n=2 for the sine-Gordon and ϕ^4 kink solitons, respectively. In both cases M is the mass parameter for the quantum fluctuations, and the scattering solutions are known:

$$\psi_k^{(1)}(x) \propto e^{ikx} [k + iM \tanh(Mx)], \tag{24}$$

$$\psi_k^{(2)}(x) \propto e^{ikx} \left[3 \tanh^2 \left(\frac{Mx}{2} \right) - 1 - \frac{4k^2}{M^2} - \frac{6ik}{M} \tanh \left(\frac{Mx}{2} \right) \right], \tag{25}$$

where the superscript is the Pöschl–Teller index n. The exponential factor indicates that we have only a right-moving plane wave. Hence the potentials are reflectionless and the phase shifts in the symmetric and anti-symmetric channels are equal. The Jost solution $(f = \mathcal{FH})$ is constructed from the above wave functions by introducing constant factors such that

$$\lim_{x \to \infty} f_k^{(n)}(x) e^{-ikx} = 1.$$

Since the wave-equation is real, both $f_k(x)$ and $f_k^*(x)$ are solutions and the Jost functions are the expansion coefficients of f and f^* for the physical scattering solution ψ_{sc} . In the antisymmetric channel the boundary conditions read

$$\lim_{x \to 0} \psi_{\rm sc}(x) = 0 \quad \text{and} \quad \lim_{x \to 0} \frac{d\psi_{\rm sc}(x)}{dx} = 1.$$

Equating the Wronskian $W[\psi_{sc}(x), f_k^{(n)}(x)]$ at spatial infinity and at $x \to 0$ immediately yields the Jost function $F_-(k) = \lim_{x\to 0} f_k(x)$ as denoted at the end of Subsec. 2.1. For the above potentials this gives

$$F_{-}^{(1)}(k) = \frac{k}{k + iM}$$
 and $F_{-}^{(2)}(k) = \frac{k - iM/2}{k + iM}$. (26)

As mentioned in footnote b, the boundary condition in the symmetric channel requires the derivative of the Jost solution such that $F_{+}(k) = \frac{1}{\mathrm{i}k} \lim_{x\to 0} \frac{df_{k}(x)}{dx}$, yielding

$$F_{+}^{(1)}(k) = \frac{k - \mathrm{i}M}{k}$$
 and $F_{+}^{(2)}(k) = \frac{k - \mathrm{i}M}{k + \mathrm{i}M/2}$. (27)

We note that $F_{+}^{(1,2)}(iM) = 0$ reflects the existence of zero modes. The analytic continuation for $F_{+}^{(1,2)}F_{-}^{(1,2)}$ is straightforward, leading to the VPE

$$\Delta E^{(1)} = \int_{M}^{\infty} \frac{dt}{2\pi} \frac{t}{\sqrt{t^2 - M^2}} \left[\ln\left(\frac{t - M}{t + M}\right) + 2\frac{M}{t} \right] = -\frac{M}{\pi},$$

$$\Delta E^{(2)} = \int_{M}^{\infty} \frac{dt}{2\pi} \frac{t}{\sqrt{t^2 - M^2}} \left[\ln\left(\frac{t - M}{t + M}\frac{2t - M}{2t + M}\right) + 3\frac{M}{t} \right] = \frac{M}{12} \left(\sqrt{3} - \frac{18}{\pi}\right). \tag{28}$$

In the above we have identified the Born subtraction as the leading term of the logarithm for large t. From the wave-equation we can show that it is indeed a single inverse power in t. We factorize $f_k(x) = \mathcal{F}_{\ell,k}(x) \mathrm{e}^{-\mathrm{i}kx}$ with the imaginary momentum wave-equation (primes are derivatives with respect to the spatial coordinate x)

$$\mathcal{F}_{it}''(x) = 2t\mathcal{F}_{it}'(x) + \sigma(x)\mathcal{F}_{\ell,it}(x)$$

and obtain the full Jost function (argument of the logarithms in Eqs. (28)) as the limit

$$F_{+}(t)F_{-}(t) = \lim_{x \to 0} \left[\mathcal{F}_{\ell,it}(x) \left(\mathcal{F}_{\ell,it}(x) - \frac{1}{t} \mathcal{F}'_{it}(x) \right) \right]. \tag{29}$$

To identify the Born approximation we expand $\mathcal{F}_{\ell,it}(x) = 1 + \mathcal{F}_1(x,t) + \cdots$ in powers of the potential σ . Integrating the differential equation for $\mathcal{F}_1(x,t)$ from the center to infinity shows that

$$\ln[F_{+}(t)F_{-}(t)] = \frac{1}{t} \int_{0}^{\infty} dx \, \sigma(x) + \mathcal{O}(\sigma^{2}). \tag{30}$$

3.2. Mass gap and thresholds

The imaginary momentum formulation is even more advantageous when there are multiple quantum fields with different masses. In the real momentum formulation, three different energy regimes must be considered: (1) bound states with energies below the smallest mass; (2) intermediate energy regime(s) between the lowest and largest masses where some modes are bound while others scatter; (3) energies above the largest mass, where all modes scatter and extend to spatial infinity.

The continuation to imaginary momenta, however, is not without obstacles. Let us explore the case with two masses $m_1 < m_2$ that have momenta $k_1 = k$ and k_2 , respectively. In the binding regime(s) they may be imaginary. For static potentials, energy is conserved and the (relativistic) dispersion relation yields $k_2^2 = k^2 + m_1^2 - m_2^2$. This may induce further branch cuts in the complex momentum plane. Within the mass gap, $0 < k^2 < m_2^2 - m_1^2$, either sign of k should produce an exponentially decaying wave function parameterized by the imaginary part of k_2 . This suggests writing $k_2 = \sqrt{k^2 + m_1^2 - m_2^2}$. In the scattering regime, $k^2 > m_2^2 - m_1^2$, the analytic continuation uses the fact that the imaginary part of the Jost function is odd for real momenta, as shown in Eq. (4). In particular, k_2 should

change sign when k does. So we would write $k_2 = k\sqrt{1 + \frac{m_1^2 - m_2^2}{k^2}}$. In Ref. 49, it has been shown that these two seemingly contradictory relations can be consistently combined as

$$k_2 = k_2(k) \equiv k \sqrt{1 + \frac{m_1^2 - m_2^2}{[k + i\epsilon]^2}} \quad \text{with } \epsilon \to 0^+.$$
 (31)

This prescription leads to additional singularities, but they occur only for momenta with negative imaginary parts, and it passes numerous consistency checks. 49 Hence it is straightforwardly permissible to analytically continue within the upper half plane with k = it and $k_2 = it_2(t) = i\sqrt{t^2 + m_2^2 - m_1^2}$. We then get the matrix differential equation

$$\mathcal{F}_{\ell,it}''(x) = 2\mathcal{F}_{\ell,it}'(x)D(t) + [M_2^2, \mathcal{F}_{\ell,it}(x)] + V(x)\mathcal{F}_{\ell,it}(x), \tag{32}$$

with $M_2 = \begin{pmatrix} m_1 & 0 \\ 0 & m_2 \end{pmatrix}$ and $D(t) = \begin{pmatrix} t & 0 \\ 0 & t_2 \end{pmatrix}$.

If the potential matrix is symmetric, V(-x) = V(x), the relevant logarithm of the Jost functions is

$$\nu(t) = \ln \det[F_S(t)F_A(t)],\tag{33}$$

where $F_S(t) = \lim_{x\to 0} [\mathcal{F}_{\ell,it}(x) - \mathcal{F}'_{\ell,it}(x)D^{-1}(t)]$ and $F_A(t) = \lim_{x\to 0} [\mathcal{F}_{\ell,it}(x)]$. In many applications the potential matrix has a skewed symmetry V(-x) $\begin{pmatrix} 1 & 0 \\ 0 & -1 \end{pmatrix}$ $V(x) \begin{pmatrix} 1 & 0 \\ 0 & -1 \end{pmatrix}$, in which case^{49,50}

$$\nu(t) = \ln \det[F_{+}(t) F_{-}(t)], \tag{34}$$

where the combinations $F_{\pm}(t) = [P_{\pm}F_S(t)D_{\mp}(t) + P_{\mp}F_A(t)D_{\pm}^{-1}(t)]$ are found using the projectors $P_+ = \begin{pmatrix} 1 & 0 \\ 0 & 0 \end{pmatrix}$ and $P_- = \begin{pmatrix} 0 & 0 \\ 0 & 1 \end{pmatrix}$ as well as the factor matrices $D_+(t) = 0$ $\begin{pmatrix} -t & 0 \\ 0 & 1 \end{pmatrix}$ and $D_{-}(t) = \begin{pmatrix} 1 & 0 \\ 0 & -t_2 \end{pmatrix}$. The Born approximation,

$$\nu^{(1)}(t) = \int_0^\infty dx \left[\frac{V_{11}(x)}{t} + \frac{V_{22}(x)}{t_2} \right],\tag{35}$$

is then subtracted from Eq. (34) to implement the no-tadpole scheme.

3.3. Instability of Shifman-Voloshin soliton

The Shifman–Voloshin soliton model extends the ϕ^4 model by adding a second scalar field χ . Its Lagrangian reads

$$\mathcal{L} = \frac{1}{2} \left[\partial_{\nu} \phi \partial^{\nu} \phi + \partial_{\nu} \chi \partial^{\nu} \chi \right] - \frac{\lambda}{4} \left[\phi^2 - \frac{M^2}{2\lambda} + \frac{\mu}{2} \chi^2 \right]^2 - \frac{\lambda}{4} \mu^2 \chi^2 \phi^2. \tag{36}$$

The Lagrangian contains a coupling constant λ and mass scale M similar to the conventional ϕ^4 model. We will discuss the meaning of the dimensionless coupling constant $\mu > 0$ shortly.

After appropriate redefinition of the fields, $(\phi, \chi) \to (M/\sqrt{2\lambda})(\phi, \chi)$ and the coordinates, $x_{\nu} \to 2x_{\nu}/M$, the rescaled Lagrangian, $\mathcal{L} \to (M^4/8\lambda)\mathcal{L}$ has a vacuum

configuration at $\phi = \pm 1$ and $\chi = 0$. We call these two possibilities the primary vacua. There are also secondary vacua at $\phi = 0$ and $\chi = \pm \sqrt{\frac{2}{\mu}}$.

For static fields the model allows a BPS construction for the classical energy of static fields

$$E_{\rm cl} = \frac{1}{2} \int_{-\infty}^{\infty} dx \left[\phi'^2 + \chi'^2 + \left(\phi^2 - 1 + \frac{\mu}{2} \chi^2 \right)^2 + \mu^2 \phi^2 \chi^2 \right]$$

$$= \frac{1}{2} \int_{-\infty}^{\infty} dx \left[\left(\phi^2 - 1 + \frac{\mu}{2} \chi^2 \pm \phi' \right)^2 + (\mu \phi \chi \pm \chi')^2 \right] \pm \left[\phi - \frac{1}{3} \phi^3 - \mu \phi \chi^2 \right]_{-\infty}^{\infty},$$
(37)

where primes denote derivatives with respect to the (dimensionless) space coordinate x. The extremal points in field space are determined from the first-order differential equations

$$\frac{d\chi(x)}{dx} = -\mu\phi(x)\chi(x) \quad \text{and} \quad \frac{d\phi(x)}{dx} = 1 - \phi^2(x) - \frac{\mu}{2}\chi^2(x). \tag{38}$$

These coupled differential equations have been studied in detail in Refs. 51 and 52. Field configurations that approach the secondary vacuum at spatial infinity have $E_{\rm cl}=0$, and we thus cannot have a soliton with this asymptotic behavior. Adopting the convention that $\lim_{x\to\pm\infty}\phi(x)=\pm 1$, we see that $\phi(x)$ is an increasing (presumably monotonically) odd function of the coordinate and χ is even, where we take the soliton center at x=0. We are free to choose $\chi(0)\geq 0$. If $\chi(0)>\sqrt{2/\mu}$, $\phi'(0)<0$ and $\chi''(0)>0$, implying that $\chi(0)$ would be a minimum. Furthermore, ϕ' would turn even more negative and not approach +1 at spatial infinity. By contradiction we thus conclude that $\sqrt{2/\mu}$ is an upper bound for $\chi(0)$ and we parameterize $\chi(0)=a\sqrt{2/\mu}$ with $0\leq a<1$, for which solitons have been constructed numerically. Observe that ϕ is in its secondary vacuum at x=0. The closer a is to unity, the larger the region in which both fields approximately equal their corresponding expectation values from the secondary vacuum. Restoring units we see from Eq. (37) that $E_{\rm cl}=\frac{4}{3}\frac{M^3}{8\lambda}=\frac{M^3}{6\lambda}$ for all solitons, independent of a.

Linearizing the time-dependent wave-equations around this soliton defines the potential and mass matrices

$$V(x) = \begin{pmatrix} \mu(1+\mu)(\phi^2 - 1) + \frac{3}{2}\mu^2\chi^2 & 2\mu(1+\mu)\chi\phi \\ 2\mu(1+\mu)\chi\phi & 6\phi^2 - 6 + \mu(\mu+1)\chi^2 \end{pmatrix} \quad \text{and} \quad (39)$$

$$M_2 = \begin{pmatrix} \mu & 0 \\ 0 & 2 \end{pmatrix},$$

respectively. Obviously V(x) is skew-symmetric and for $\mu \leq 2$ we can directly apply the formalism of Subsec. 3.2, while for $\mu > 2$ we first need to swap the diagonal elements of both V(x) and M_2 . Selected results for the VPE from Ref. 50 are listed in Table 1. Except for $\mu = 2$, where the model is equivalent to two identical ϕ^4 kinks,

-3.406

-4.076

0.99999

-2.900

-1.284

soliton, measured in units of M.							
a μ	0.5	1.6	2.0	2.8	3.6	4.0	4.4
0.0	-0.830	-1.186	-1.333	-1.661	-2.039	-2.246	-2.467
0.1	-0.833	-1.186	-1.333	-1.661	-2.038	-2.246	-2.467
0.5	-0.906	-1.195	-1.333	-1.654	-2.036	-2.249	-2.477
0.9	-1.229	-1.217	-1.333	-1.666	-2.112	-2.372	-2.656
0.99	-1.661	-1.235	-1.333	-1.714	-2.284	-2.628	-3.008
0.999	-2.076	-1.251	-1.333	-1.764	-2.459	-2.888	-3.364
0.9999	-2.488	-1.268	-1.333	-1.813	-2.634	-3.147	-3.720

-1.863

-2.809

-1.333

Table 1. Numerical results for the vacuum polarization energy of the Shifman–Voloshin soliton, measured in units of M.

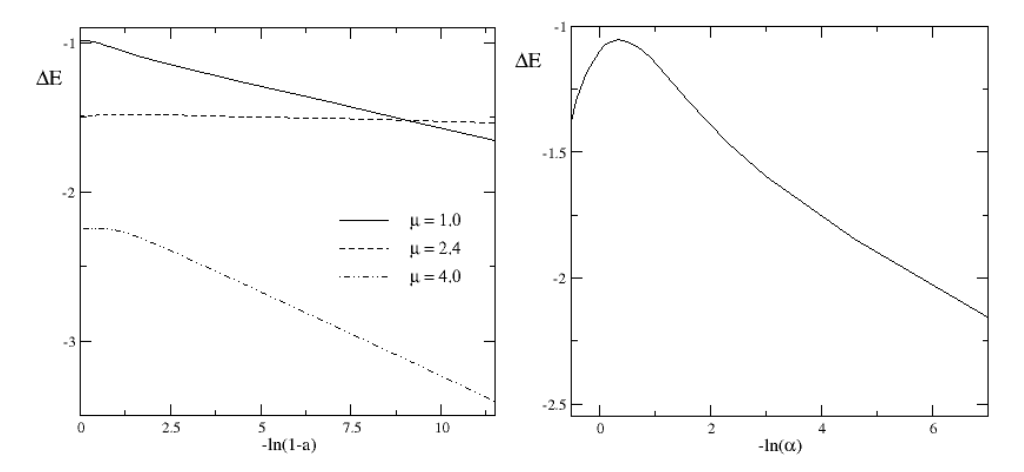


Fig. 1. VPE of the Shifman–Voloshin soliton for various model parameters μ as functions of the variational parameter a (left panel) and the ϕ^6 model soliton as a function of the model parameter α (right panel).

the VPE is unbounded from below as $a \to 1$. A numerical fit exhibits a logarithmic divergence: $\Delta E \sim E_0 + E_1 \ln(1-a)$, with $E_{1,2}$ approximately independent of a. This behavior is shown in the left panel of Fig. 1.

Hence for any given λ , there will be an a close to unity such that the total energy is negative. By extending into the secondary vacuum the soliton is destabilized at the one-loop quantum level. For this to happen, the curvatures of the field potential at the primary and the (degenerate) secondary vacua must be different; recall that for $\mu = 2$ they are equal, and then there is no instability.

3.4. Further quantum instabilities: Higher power field potentials

Models with higher than quartic powers in the field potential may also possess primary and secondary vacua for certain parameters. An example is the

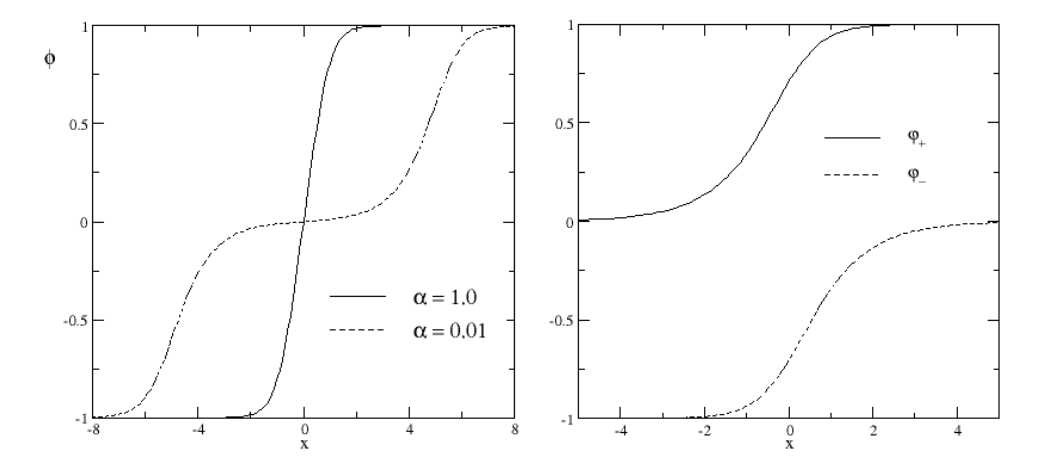


Fig. 2. The soliton profiles of the φ^6 model. Note that $\alpha = 0$ in the right panel.

Lagrangian

$$\mathcal{L} = \frac{1}{\lambda} \left[\frac{1}{2} \partial_{\nu} \varphi \partial^{\nu} \varphi - U(\varphi) \right] \quad \text{with } U(\varphi) = \frac{1}{2} (\varphi^2 - 1)^2 (\varphi^2 + \alpha^2). \tag{40}$$

For nonzero values of the model parameter α , only primary vacua at $\varphi = \pm 1$ exist. As shown in Fig. 2, solitons mediate between these two values as the spatial coordinate varies between negative and positive infinity. 53,54 The potential for the harmonic fluctuations around this soliton is invariant under spatial reflection and the VPE can be straightforwardly computed using the methods described above, via Eq. (29). The right panel in Fig. 1 shows that for $\alpha \to 0$, the VPE approaches negative infinity like $\ln \alpha$. ^{55,56} On the other hand, the classical energy is always finite and positive. Classical and quantum energies contribute with different powers of the loop counting parameter λ , which appears as an overall factor in \mathcal{L} . Hence there will always be a value of λ such that the total energy is positive and the soliton is stable. The situation changes drastically for $\alpha = 0$. Then a secondary vacuum emerges at $\varphi = 0$ and two soliton solutions φ_{\pm} exist that link $\varphi = 0$ with $\varphi = 1$ and $\varphi = -1$ with $\varphi = 0$, respectively. Actually for a tiny but nonzero α , the soliton from above can be viewed as a combination of these two solutions whose separation increases as $\alpha \to 0$. This may also be inferred from the profile functions shown in Fig. 2.

Obviously the curvatures of the field potential at $\varphi = 0$ and $\varphi = \pm 1$ differ. Hence the masses of the quantum fluctuations at positive and negative infinity are also different. Even though an imaginary momentum formalism has not (yet) been developed for this scenario, the reflection and transmission coefficients as well as the bound state energies have been computed both analytically⁵³ and numerically⁵⁵ so that the VPE can be obtained from Eq. (11). That simulation reveals a translational dependence. With x_0 being the center of the soliton, the VPE is observed to change by approximately 0.101 per unit of x_0 . The same variation is found for the VPE of a

background potential built from a barrier of width x_0 and a height determined from the difference of the two curvatures. In contrast to α , x_0 is a variational parameter that describes the shape of the soliton and for any given λ we can choose x_0 such that the total energy is negative. Hence the $\alpha=0$ soliton is unstable at one-loop order. Of course, this picture is consistent with the $\alpha \to 0$ divergence of the VPE discussed above, when the soliton configuration exhibits two well-separated $\alpha\equiv 0$ structures. The same kind of instability has been observed in the φ^8 model.⁵⁷

4. Fermions and Cosmic Strings

In contrast to the Abelian vortices that we will discuss in Sec. 5, string configurations that are embedded in SU(2) Higgs-gauge theory are not stable by their topological structure, so it is of interest to explore whether quantum effects may lead to stabilization. For large N (the number of internal fermion degrees of freedom in the field theory) the fermion contribution will be dominant.

For the current investigation the fermion doublet will be assumed degenerate, so that the introduction of a matrix notation for the Higgs field is appropriate. In general the isospin group SU(2) is described by three Euler angles. One angle picks up the winding of the string in azimuthal direction. So we are left with two angles ξ_1 and ξ_2 that parameterize the isospin orientation.⁵⁸ They will later be treated as variational parameters. For notational simplicity, we introduce the abbreviations $s_i = \sin(\xi_i)$ and $c_i = \cos(\xi_i)$. Then the string configuration reads

$$\Phi = \begin{pmatrix} \phi_0^* & \phi_+ \\ -\phi_+^* & \phi_0 \end{pmatrix} = v f_H(\rho) \begin{pmatrix} s_1 s_2 e^{-in\varphi} & -ic_1 - s_1 c_2 \\ -ic_1 + s_1 c_2 & s_1 s_2 e^{in\varphi} \end{pmatrix}$$
(41)

for the Higgs field and

$$\mathbf{W} = n \, s_1 \, s_2 \, \frac{f_G(\rho)}{g\rho} \, \hat{\varphi} \begin{pmatrix} s_1 s_2 & -(ic_1 + s_1 c_2) e^{in\varphi} \\ (ic_1 - s_1 c_2) e^{-in\varphi} & -s_1 s_2 \end{pmatrix}$$
(42)

for the gauge boson (in temporal gauge with $W_0 = 0$). The variables ρ and φ are polar coordinates in the plane perpendicular to the string, while the gauge coupling constant g and the Higgs vacuum expectation value v are model parameters. The profile functions f_H and f_G are subject to the boundary conditions

$$f_G, f_H \to 0 \quad \text{for } \rho \to 0 \quad \text{and} \quad f_G, f_H \to 1 \quad \text{for } \rho \to \infty.$$
 (43)

In the numerical simulations the winding number of the string will be taken as n = 1

Since the Weinberg angle vanishes in this model, the gauge symmetry is $SU(2)_L$ while the U(1) hypercharge decouples and the three gauge bosons are degenerate. The boson part of the Lagrangian reads

$$\mathcal{L}_{\text{bos}} = -\frac{1}{2} \text{tr}(G^{\mu\nu}G_{\mu\nu}) + \frac{1}{2} \text{tr}(D^{\mu}\Phi)^{\dagger}D_{\mu}\Phi - \frac{\lambda}{2} \text{tr}(\Phi^{\dagger}\Phi - v^{2})^{2}, \tag{44}$$

with the covariant derivative $D_{\mu} = \partial_{\mu} - igW_{\mu}$ and the SU(2) field strength tensor

$$G_{\mu\nu} = \partial_{\mu} W_{\nu} - \partial_{\nu} W_{\mu} - ig[W_{\mu}, W_{\nu}]. \tag{45}$$

The boson masses are determined from g and v and the Higgs self-coupling λ as $m_{\rm W}=gv/\sqrt{2}$ and $m_{\rm H}=2v\sqrt{\lambda}$ for the gauge and Higgs bosons, respectively. The interaction with the degenerate fermion doublet is described by the Lagrangian

$$\mathcal{L}_{\text{fer}} = i\overline{\Psi}(P_L D + P_R \partial)\Psi - f\overline{\Psi}(\Phi P_R + \Phi^{\dagger} P_L)\Psi, \tag{46}$$

with the right/left-handed projectors $P_{R,L} = (\mathbb{1} \pm \gamma_5)/2$. Upon spontaneous symmetry breaking, the Yukawa coupling f induces a fermion mass m = vf. Assuming a heavy fermion doublet with the mass of the top quark, the Standard Model suggests the parameters

$$g = 0.72, \quad v = 177 \text{ GeV}, \quad m_{\text{H}} = 140 \text{ GeV}, \quad f = 0.99.$$
 (47)

In the numerical search for a stable string, later other values for the Yukawa coupling will be considered as well.

The classical energy per unit length of the string is determined by $\mathcal{L}_{\mathrm{bos}}$

$$\frac{E_{\rm cl}}{m^2} = 2\pi \int_0^\infty \rho \, d\rho \, \left\{ n^2 s_1^2 s_2^2 \left[\frac{2}{g^2} \left(\frac{f_G'}{\rho} \right)^2 + \frac{f_H^2}{f^2 \rho^2} (1 - f_G)^2 \right] + \frac{f_H'^2}{f^2} + \frac{\mu_H^2}{4f^2} (1 - f_H^2)^2 \right\}, \tag{48}$$

where the dimensionless radial integration variable is related to the physical radius by $\rho_{\text{phys}} = \rho/m$, and we have introduced the mass ratio $\mu_H \equiv m_H/m$.

4.1. Choice of Gauge and the Dirac equation

An additional problem arising for string configurations with winding in gauge theories is that the string does not induce a well-behaved Born series when expanding in powers of the interaction term, $H_{\rm int}$ from Eq. (46); see also Eq. (51). Even though the full Hamiltonian is gauge invariant, $H_{\rm int}$ is not and does not vanish at spatial infinity. This obstacle appears because the Dirac Hamiltonian that is obtained by straightforward substitution of the string background, Eqs. (41) and (42), does not turn into the free Dirac Hamiltonian at $\rho \to \infty$. Instead it becomes $H \to U^{\dagger}(\varphi)H_{\rm free}U(\varphi)$, where $U(\varphi)$ is a local gauge transformation reflecting the string winding. It acts only on the left-handed fermions

$$U(\varphi) = P_L \exp(i\hat{\boldsymbol{n}}(\varphi) \cdot \boldsymbol{\tau} \, \xi_1) + P_R \quad \text{with } \hat{\boldsymbol{n}}(\varphi) = \begin{pmatrix} s_2 \cos(n\varphi) \\ -s_2 \sin(n\varphi) \\ c_2 \end{pmatrix}. \tag{49}$$

Unfortunately, making the obvious gauge transformation $H \to U(\varphi)HU^{\dagger}(\varphi)$ does not solve the problem: Although it would generate vanishing interactions at infinity, it will also induce a $1/\rho^2$ potential at the core of the string, $\rho \to 0$. This choice might still yield well-defined phase shifts, though they would likely be difficult to compute

numerically, and the conditions underlying the analyticity of the scattering data could be violated by this singular behavior; see, however, Subsec. 5.3. As we saw at the end of the previous section, analyticity is central for numerical feasibility of our approach. As a solution, we can define a radially extended gauge transformation

$$U(\rho, \varphi) = P_L \exp(i\hat{\mathbf{n}} \cdot \boldsymbol{\tau} \, \xi(\rho)) + P_R. \tag{50}$$

This transformation fixes the gauge and gives the interaction part of the Dirac Hamiltonian as

$$H_{\text{int}} = m \left[(f_H c_\Delta - 1) \begin{pmatrix} 1 & 0 \\ 0 & -1 \end{pmatrix} + i f_H s_\Delta \begin{pmatrix} 0 & 1 \\ -1 & 0 \end{pmatrix} \hat{\boldsymbol{n}} \cdot \boldsymbol{\tau} \right]$$

$$+ \frac{\partial \xi}{2\partial \rho} \begin{pmatrix} -\boldsymbol{\sigma} \cdot \hat{\boldsymbol{\rho}} & \boldsymbol{\sigma} \cdot \hat{\boldsymbol{\rho}} \\ \boldsymbol{\sigma} \cdot \hat{\boldsymbol{\rho}} & -\boldsymbol{\sigma} \cdot \hat{\boldsymbol{\rho}} \end{pmatrix} \hat{\boldsymbol{n}} \cdot \boldsymbol{\tau} + \frac{n s_2}{2\rho} \begin{pmatrix} -\boldsymbol{\sigma} \cdot \hat{\boldsymbol{\varphi}} & \boldsymbol{\sigma} \cdot \hat{\boldsymbol{\varphi}} \\ \boldsymbol{\sigma} \cdot \hat{\boldsymbol{\varphi}} & -\boldsymbol{\sigma} \cdot \hat{\boldsymbol{\varphi}} \end{pmatrix}$$

$$\times \left[f_G s_\Delta I_G(\Delta) + (f_G - 1) s_\xi I_G(-\xi) \right], \tag{51}$$

where, as above, we abbreviate $s_{\Delta} = \sin(\Delta(\rho))$, $s_{\xi} = \sin(\xi(\rho))$, etc. The new gauge function $\xi(\rho)$ appears via the difference $\Delta(\rho) \equiv \xi_1 - \xi(\rho)$ while the isospin matrices are

$$\hat{\boldsymbol{n}} \cdot \boldsymbol{\tau} = \begin{pmatrix} c_2 & s_2 e^{\mathrm{i}n\varphi} \\ s_2 e^{-\mathrm{i}n\varphi} & -c_2 \end{pmatrix} \quad \text{and}$$

$$I_G(x) = \begin{pmatrix} -s_2 s_x & (c_2 s_x - \mathrm{i}c_x) e^{\mathrm{i}n\varphi} \\ (c_2 s_x + \mathrm{i}c_x) e^{-\mathrm{i}n\varphi} & s_2 s_x \end{pmatrix}.$$
(52)

Imposing the boundary conditions $\xi(0) = 0$ and $\xi(\infty) = \xi_1$ for the new gauge function $\xi(\rho)$ defines a well-behaved scattering problem. The specific form of $\xi(\rho)$ is irrelevant (apart from its boundary conditions) and must not have any influence on the quantum energy, since it merely parameterizes a gauge transformation.

Note that the gauge transformation is single-valued at spatial infinity, $U(\infty, \varphi) = U(\infty, \varphi + 2\pi)$. In this respect it differs from the analogous problem of fractional magnetic fluxes in QED. In that case a similar choice of gauge would not be a remedy; rather the calculation of the vacuum polarization energy requires the introduction of a return flux.⁵⁹ This approach can also be used for the present calculation, but it is much more laborious numerically.^{60,61}

We introduce grand-spin type states that couple spin and isospin to account for the angular dependence. For fixed angular momentum ℓ there are four of them,

$$\begin{split} \langle \varphi; SI | \ell + + \rangle &= \mathrm{e}^{i(\ell+n)\varphi} \binom{1}{0}_S \otimes \binom{1}{0}_I \quad \langle \varphi; SI | \ell + - \rangle = -\mathrm{i} \, \mathrm{e}^{i\ell\varphi} \binom{1}{0}_S \otimes \binom{0}{1}_I, \\ \langle \varphi; SI | \ell - + \rangle &= \mathrm{i} \, \mathrm{e}^{i(\ell+n+1)\varphi} \binom{0}{1}_S \otimes \binom{1}{0}_I \quad \langle \varphi; SI | \ell - - \rangle = \mathrm{e}^{i(\ell+1)\varphi} \binom{0}{1}_S \otimes \binom{0}{1}_I, \end{split}$$

where S and I refer to the spin and isospin subspaces, respectively. These grandspin states serve to construct four-component Dirac spinors in coordinate space

$$\langle \rho | + + \rangle = \begin{pmatrix} f_1(\rho) | \ell + + \rangle \\ g_1(\rho) | \ell - + \rangle \end{pmatrix} \quad \langle \rho | + - \rangle = \begin{pmatrix} f_2(\rho) | \ell + - \rangle \\ g_2(\rho) | \ell - - \rangle \end{pmatrix},$$

$$\langle \rho | - + \rangle = \begin{pmatrix} f_3(\rho) | \ell - + \rangle \\ g_3(\rho) | \ell + + \rangle \end{pmatrix} \quad \langle \rho | - - \rangle = \begin{pmatrix} f_4(\rho) | \ell - - \rangle \\ g_4(\rho) | \ell + - \rangle \end{pmatrix},$$
(54)

where we have suppressed the angular momentum index of the radial functions because the Dirac equation is diagonal in this quantum number. We combine these eight radial functions into two vectors $\mathbf{f} = \sum_{i=1}^4 f_i(\rho)\hat{e}_i$ and $\mathbf{g} = \sum_{i=1}^4 g_i(\rho)\hat{e}_i$ to write the Dirac equation as a set of eight coupled first-order linear differential equations in the matrix form

$$(E - m) \mathbf{f} = V_{uu} \mathbf{f} + (D_u + V_{ud}) \mathbf{g},$$

$$(E + m) \mathbf{g} = (D_d + V_{du}) \mathbf{f} + V_{dd} \mathbf{g}.$$
(55)

The derivative operators are fully contained in the diagonal matrices

$$D_{u} = \operatorname{diag}\left(\partial_{\rho} + \frac{\ell + n + 1}{\rho}, \partial_{\rho} + \frac{\ell + 1}{\rho}, -\partial_{\rho} + \frac{\ell + n}{\rho}, -\partial_{\rho} + \frac{\ell}{\rho}\right),$$

$$D_{d} = \operatorname{diag}\left(-\partial_{\rho} + \frac{\ell + n}{\rho}, -\partial_{\rho} + \frac{\ell}{\rho}, \partial_{\rho} + \frac{\ell + n + 1}{\rho}, \partial_{\rho} + \frac{\ell + 1}{\rho}\right).$$
(56)

We will give the explicit form of the real 4×4 matrices V_i in terms of the radial functions when we set up the Born series for the scattering data. Here it suffices to note that these matrices vanish at spatial infinity, so the asymptotic solutions are cylindrical Bessel and Hankel functions. In particular, the Hankel functions

$$\mathcal{H}_{u} = \operatorname{diag}(H_{\ell+n}^{(1)}(k\rho), H_{\ell}^{(1)}(k\rho), H_{\ell+n+1}^{(1)}(k\rho), H_{\ell+1}^{(1)}(k\rho)),$$

$$\mathcal{H}_{d} = \operatorname{diag}(H_{\ell+n+1}^{(1)}(k\rho), H_{\ell+1}^{(1)}(k\rho), H_{\ell+n}^{(1)}(k\rho), H_{\ell}^{(1)}(k\rho)),$$
(57)

that parameterize the outgoing asymptotic fields with (radial) momentum k can be used to set up the scattering problem via the matrix generalization

$$\mathbf{f} \longrightarrow \mathcal{F} \cdot \mathcal{H}_u \quad \text{and} \quad \mathbf{g} \longrightarrow \kappa \, \mathcal{G} \cdot \mathcal{H}_d,$$
 (58)

where $\kappa = \frac{k}{E+m} = \frac{E-m}{k}$. For simplicity we have not written out that the matrices \mathcal{F} , \mathcal{G} and $\mathcal{H}_{u,d}$ are functions of both the radial coordinate ρ and the momentum k. The boundary conditions for the 4×4 complex matrices \mathcal{F} and \mathcal{G} are simply $\lim_{\rho\to\infty} \mathcal{F} = 1$ and $\lim_{\rho\to\infty} \mathcal{G} = 1$, so the various columns of the above products refer to outgoing waves in different grand spin channels.

The interaction Hamiltonian, Eq. (51), anti-commutes with the Dirac matrix α_3 . Hence the spectrum is symmetric and we only need to consider the case with

 $E = +\sqrt{k^2 + m^2}$ after analytic continuation to k = it. This continuation turns the Hankel functions into modified Hankel functions $K_{\ell}(z)$ and we define

$$Y_{u} = \operatorname{diag}\left(\frac{K_{\ell+n}(t\rho)}{K_{\ell+n+1}(t\rho)}, \frac{K_{\ell}(t\rho)}{K_{\ell+1}(t\rho)}, -\frac{K_{\ell+n+1}(t\rho)}{K_{\ell+n}(t\rho)}, -\frac{K_{\ell+1}(t\rho)}{K_{\ell}(t\rho)}\right) = -(Y_{d})^{-1}.$$
(59)

Furthermore, we rewrite the kinematic coefficient $\kappa \to z_{\kappa}$ as

$$z_{\kappa} = \frac{m + i\tau}{t}$$
, with $\tau = \sqrt{t^2 - m^2}$, (60)

so that z_{κ} is a pure phase.

The coupled first-order differential equations take the form

$$\partial_{\rho} \mathcal{F} = [\mathcal{Q}_{ff} + O_d] \cdot \mathcal{F} + \mathcal{F} \cdot \mathcal{Q}_{ff}^{(r)} - t[\mathcal{Q}_{fg} + C] \cdot \mathcal{G} \cdot Y_d,$$

$$\partial_{\rho} \mathcal{G} = [\mathcal{Q}_{gg} + O_u] \cdot \mathcal{G} + \mathcal{G} \cdot \mathcal{Q}_{gg}^{(r)} - t[\mathcal{Q}_{gf} - C] \cdot \mathcal{F} \cdot Y_u,$$
(61)

where the purely kinematical matrices are also straightforwardly expressed as

$$Q_{ff}^{(r)} = tC \cdot Y_d(k) - O_d \quad \text{and} \quad Q_{gg}^{(r)} = -tC \cdot Y_u(k) - O_u. \tag{62}$$

The first set of matrices reads

$$Q_{gg} = \overline{\mathcal{M}}_{gg} = \begin{pmatrix} G & P \\ -P & -G^{\dagger} \end{pmatrix} \quad \text{and} \quad Q_{ff} = \overline{\mathcal{M}}_{ff} = \begin{pmatrix} -G^{\dagger} & P \\ -P & G \end{pmatrix},$$
 (63)

while the matrices involving the energy are

$$Q_{fg} = \frac{1}{m + i\tau} \begin{pmatrix} -H & G^{\dagger} \\ -G & H \end{pmatrix} \quad \text{and} \quad Q_{gf} = \frac{1}{m - i\tau} \begin{pmatrix} H & G \\ -G^{\dagger} & -H \end{pmatrix}. \tag{64}$$

In the above we have conveniently introduced 2×2 sub-matrices

$$H = \alpha_H \begin{pmatrix} 1 & 0 \\ 0 & 1 \end{pmatrix}, \quad P = \alpha_P \begin{pmatrix} -ic_2 & -s_2 \\ s_2 & ic_2 \end{pmatrix} = -P^{\dagger}, \quad \text{and}$$

$$G = \alpha_G \begin{pmatrix} s_2 s_{\Delta} & c_{\Delta} + ic_2 s_{\Delta} \\ c_{\Delta} - ic_2 s_{\Delta} & -s_2 s_{\Delta} \end{pmatrix} + \alpha_{\xi} \begin{pmatrix} -s_2 s_{\xi} & c_{\xi} - ic_2 s_{\xi} \\ c_{\xi} + ic_2 s_{\xi} & s_2 s_{\xi} \end{pmatrix}$$

$$+ \alpha_r \begin{pmatrix} -ic_2 & -s_2 \\ s_2 & ic_2 \end{pmatrix}.$$

$$(65)$$

The α factors contain the profile functions

$$\alpha_r(\rho) = \frac{1}{2} \frac{\partial \xi(\rho)}{\partial \rho}, \quad \alpha_G(\rho) = \frac{ns_2}{2\rho} f_G(\rho) s_{\Delta}, \quad \alpha_{\xi}(\rho) = \frac{ns_2}{2\rho} [f_G(\rho) - 1] s_{\xi},$$

$$\alpha_H(\rho) = m[f_H(\rho) c_{\Delta} - 1] \quad \text{and} \quad \alpha_P(\rho) = m f_H(\rho) s_{\Delta}.$$
(66)

We are not yet at the point to compute the Jost function as the logarithm of the determinant of \mathcal{F} (or \mathcal{G}). These determinants are in general not real, but rather are complex conjugate to each other. This is related to the fact that the (free) spinors explicitly contain mass factors that differ at $\rho = 0$ and $\rho \to \infty$. For real momentum, a typical solution in the vicinity of $\rho = 0$ looks like⁶²

$$\binom{f_4}{g_4} \sim \left(\frac{k}{q}\right)^l \left(\frac{\sqrt{E + mcf_H(0)} J_l(q\rho)}{\sqrt{E - mcf_H(0)} J_{l+1}(q\rho)}\right),$$
 (67)

with $q = \sqrt{E^2 - (mcf_H(0))^2}$, and similar dependencies hold for the other six radial functions. These square-root coefficients lead to a definition of the Jost function as⁶⁰

$$\exp[\nu(t)] = \left(\frac{\tau - \mathrm{i}m}{\tau - \mathrm{i}mcf_H(0)}\right)^2 \lim_{\rho \to 0} \det(\mathcal{F}) = \left(\frac{\tau + \mathrm{i}m}{\tau + \mathrm{i}mcf_H(0)}\right)^2 \lim_{\rho \to 0} \det(\mathcal{G}). \tag{68}$$

The power of two occurs because we compute the determinant of a 4×4 matrix. Note that this redefinition not only cancels the imaginary parts, but also modifies the real part. Furthermore, it cancels the logarithmic singularity in $\ln \lim_{\rho \to 0} \det(\mathcal{F})$ observed numerically at $t \sim m$. Since f_H is part of the interaction, this correction factor also undergoes expansion in the framework of the Born series. The Born series for $\det(\mathcal{F})$ is constructed by iterating the differential equations of Eq. (61) in $\overline{\mathcal{M}}_i$; see Ref. 44 for more details.

4.2. Numerical set-up

Thus far we have addressed the technical obstacles related to the singular structure of the string at the origin. Despite the additional simplification due to the use of a fake boson subtraction as in Eq. (22) for the subleading logarithmic divergences, the numerical computation is still expensive. The scattering data are extracted from a multi-channel problem and, for the final result to be reliable, several hundred partial wave channels must be included. Furthermore, channels that contain orbital angular momentum $\ell=0$ require disentangling a constant from a logarithm for the regular and irregular solutions when $\rho=\rho_{\rm min}\to 0$. This is only possible by extrapolating a fit of the form

$$\det(\mathcal{F}) = a_0 + \frac{a_1}{\ln(\rho_{\min})} + \frac{a_2}{\ln^2(\rho_{\min})} \cdots \longrightarrow a_0, \tag{69}$$

for the Jost function in these channels. These numerical efforts restrict the number of variational parameters that can be used to characterize the profile functions. In addition to ξ_1 and ξ_2 , we introduce three scale parameters w_H , w_W and w_ξ via the ansätze

$$f_H(\rho) = 1 - e^{-\rho/w_H}, \quad f_G(\rho) = 1 - e^{-(\rho/w_G)^2}, \quad \xi(\rho) = \xi_1[1 - e^{-(\rho/w_\xi)^2}].$$
 (70)

Table 2. Numerical results for the fermion vacuum polarization energy ΔE adapted from Ref. 61 for $w_G = w_H = 2.0$ and $\xi_1 = 0.4\pi$. The second row shows the contribution from the renormalized Feynman diagrams in the minimal subtraction scheme (including the fake boson piece) while E_{scat} denotes the scattering momentum integral. The last two lines originate from an adjusted large t treatment of the integral for E_{scat} , see text.

$\overline{w_{\xi}}$	1.0	2.0	3.0	4.0
$\overline{E_{\mathrm{FD}}}$	-0.0623	-0.0320	-0.0264	-0.0222
$E_{\rm scat}, \alpha = 2.0$	0.1606	0.1294	0.1235	0.1193
ΔE	0.0983	0.0974	0.0971	0.0971
$E_{\rm scat}, \alpha = 2.4$	0.1588	0.1280	0.1222	0.1188
ΔE	0.0964	0.0960	0.0958	0.0959

The scale w_{ξ} parameterizes the shape of the gauge profile, which should not be observable as discussed above. The radial dependencies of the profiles are chosen to keep $E_{\rm cl}$ regular. In Ref. 44 other parameterizations for $f_G(\rho)$ have also been considered. No substantial differences for the VPE were observed.

In what follows, we write the VPE as the sum

$$\Delta E = E_{\text{scat}} + E_{\text{FD}},\tag{71}$$

where E_{scat} is the momentum integral as in Eq. (22) and E_{FD} is the combination of all Feynman diagrams with the counterterms.

4.3. Gauge invariance

We check gauge invariance by varying the shape of the gauge profile, $\xi(\rho)$. Typical results are shown in Table 2. As expected, the individual contributions to ΔE depend strongly on w_{ξ} . However, these changes cancel out almost completely. Numerically the most cumbersome part of the calculation is $E_{\rm scat}$. From various numerical considerations (change of extrapolation scheme for the partial wave sum, modification of the momentum integration grid, etc.), its numerical accuracy is estimated to be at the 1% level. An example for the accuracy test is presented in the last two lines of Table 2. The large t contribution to the integral in Eq. (21) is computed by fitting an inverse power to the integrand: $\frac{1}{t^{\alpha}}$. The large mass expansion of the Feynman diagrams yields $\alpha = 2.0$, while a numerical fit has a slightly larger value $\alpha \approx 2.4$, most likely because subleading powers are not fully negligible. Within that range of numerical uncertainty of $E_{\rm scat}$, ΔE is indeed independent of w_{ξ} .

4.4. Results for on-shell renormalization

The results in Table 2 were obtained in the $\overline{\rm MS}$ renormalization scheme, which essentially omits finite terms introduced with renormalizing the Feynman diagrams. Any other scheme merely differs by manifestly gauge invariant, finite counterterms. To obtain physically meaningful results, we need to impose renormalization conditions that correspond to a particle interpretation. To be specific, we consider the

so-called *on-shell* scheme, in which the coefficients of the four allowed counterterms are determined such that

- the tadpole graph vanishes
- the Higgs mass remains unchanged
- the normalization of Higgs particle remains unchanged
- and the normalization of vector meson remains unchanged

in the presence of fermionic quantum corrections. Explicit expressions for the corresponding counterterms are listed in Ref. 44, and a similar calculation is sketched in Subsec. 5.4. Note that the vector meson mass M_W is not fixed by these conditions and thus will be a prediction that includes quantum corrections. Hence, we tune the gauge coupling to reproduce the physical value $M_W \approx 90$ GeV.

4.4.1.
$$\xi_2 = \frac{\pi}{2}$$

In a first step we consider the particular case $\xi_2 = \frac{\pi}{2}$, for which the Dirac Hamiltonian not only is Hermitian but also yields real matrix elements in Eq. (65).

In Fig. 3, we show results for the vacuum polarization energy per unit length. The wider the background fields, the weaker the dependence on the angle ξ_1 . The vacuum polarization per unit length is quite small. Even for large widths, it does not exceed a fraction of the fermion mass squared. With the exception of very small widths, the vacuum polarization turns out to be positive. Hence there is no indication that the fermion vacuum polarization energy alone can stabilize cosmic strings, since the classical energy is larger by orders of magnitude unless the coupling

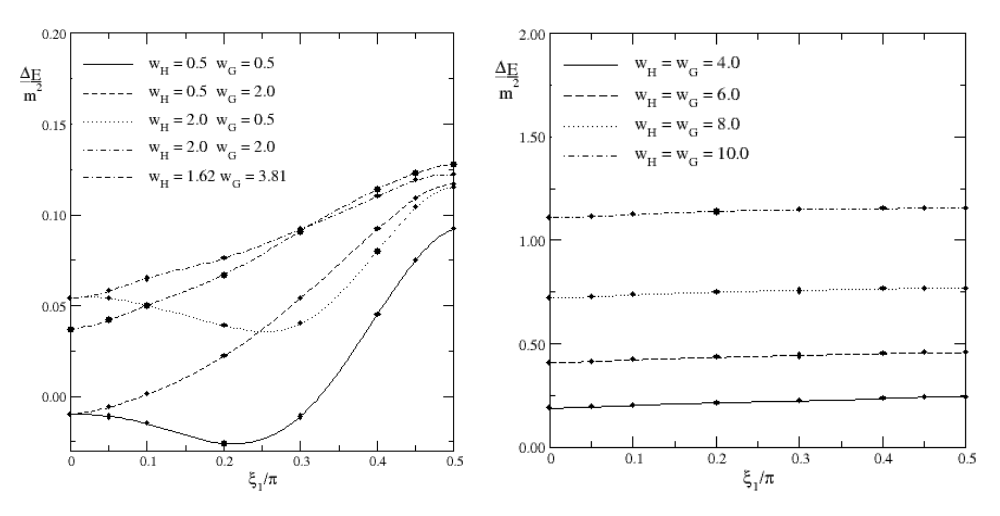


Fig. 3. Vacuum polarization energy as a function of the angle ξ_1 for different values of the width parameters w_H and w_G in the on-shell renormalization scheme. The physically motivated model parameters, Eq. (47), are used. The dots refer to actual computations, while the lines stem from a cubic spline. These results do not include the combinatoric color factor N.

constants are $f, g \sim \mathcal{O}(10)$, which would bring the dominating Fourier components of the profiles into the vicinity of the Landau ghost pole. Hence any such binding would be obscured by the existence of the Landau ghost, which arises when including quantum corrections in a manner that does not reflect asymptotic freedom. Here it is due to the omission of quantum corrections from fluctuating gauge boson fields. The estimate for the Landau ghost contribution discussed in Ref. 44 suggests that the issue can be safely ignored for $f, g \lesssim 5$.

4.4.2. Isospin invariance

Alternatively, the field configuration in Eqs. (41) and (42) can be written as

$$\begin{pmatrix} \phi_{+}(\rho,\varphi) \\ \phi_{0}(\rho,\varphi) \end{pmatrix} = f_{H}(\rho)U(\xi_{1},\xi_{2},\varphi) \begin{pmatrix} 0 \\ v \end{pmatrix} \quad \text{and}$$

$$\mathbf{W}(\rho,\varphi) = \frac{1}{g} \frac{\hat{\varphi}}{\rho} f_{G}(\rho) U(\xi_{1},\xi_{2},\varphi) \partial_{\varphi} U^{\dagger}(\xi_{1},\xi_{2},\varphi).$$

$$(72)$$

This formulation has introduced the SU(2) matrix

$$U(\xi_1, \xi_2, \varphi) = n_0 \mathbb{1} - i \boldsymbol{n} \cdot \boldsymbol{\tau} \quad \text{with } \hat{\boldsymbol{n}}_4(\xi_1, \xi_2, \varphi) = \begin{pmatrix} \sin \xi_1 \sin \xi_2 \cos \varphi \\ \cos \xi_1 \\ \sin \xi_1 \cos \xi_2 \\ \sin \xi_1 \sin \xi_2 \sin \varphi \end{pmatrix}. \tag{73}$$

A global rotation within the plane of the second and third component by the angle α with $\tan \alpha = s_1 c_2/c_1$ transforms the four-component unit vector $\hat{\boldsymbol{n}}_4$ into

$$\widetilde{n}_4(\xi_1, \xi_2, \varphi) = \begin{pmatrix} s_1 s_2 \cos \varphi \\ \sqrt{1 - s_1^2 s_2^2} \\ 0 \\ s_1 s_2 \sin \varphi \end{pmatrix}.$$
(74)

Hence observables (which are, by definition, gauge invariant) will not depend on the two angles ξ_1 and ξ_2 individually but only on the product s_1s_2 . Said another way, all observables must remain invariant along paths of constant s_1s_2 in isospin space.⁶³ This invariance is not manifest for our calculation of the VPE. For example, the local gauge transformation, Eq. (50), does not exhibit that invariance. Neither the individual Feynman diagrams that are added back for the subtraction of Born terms nor the fake boson method are subject to that symmetry. We therefore have to verify that invariance from the numerical simulation of the full VPE.

From the sample calculations listed in Table 3 we see that the variation in ΔE along a path with constant s_1s_2 is as small as a quarter of a percent, while the absolute values of the various contributions vary on the order of 20%.

The simplest check of two configurations with the same s_1s_2 is just to swap the two angles. Results of that operation are shown in the left panel of Fig. 4 for several

Table 3. Contributions to Eq. (71) and their variation with the isospin angles. In all cases we have $s_1s_2\approx 0.29389$. The width parameters of the boson profiles are $w_G=w_H=3.5$. The results were obtained with various values for the widths of the gauge function and fake boson profiles.

$\overline{\xi_1/\pi}$	ξ_2/π	$E_{\rm scat}$	$E_{ m FD}$	ΔE	$ E_{\rm scat} + E_{ m FD} $
0.1	0.4	0.1504	0.0014	0.1518	0.1518
0.4	0.1	0.1702	-0.0180	0.1521	0.1882
0.3	0.11834	0.1496	0.0021	0.1517	0.1517
0.2	1/6	0.1639	-0.0117	0.1522	0.1758

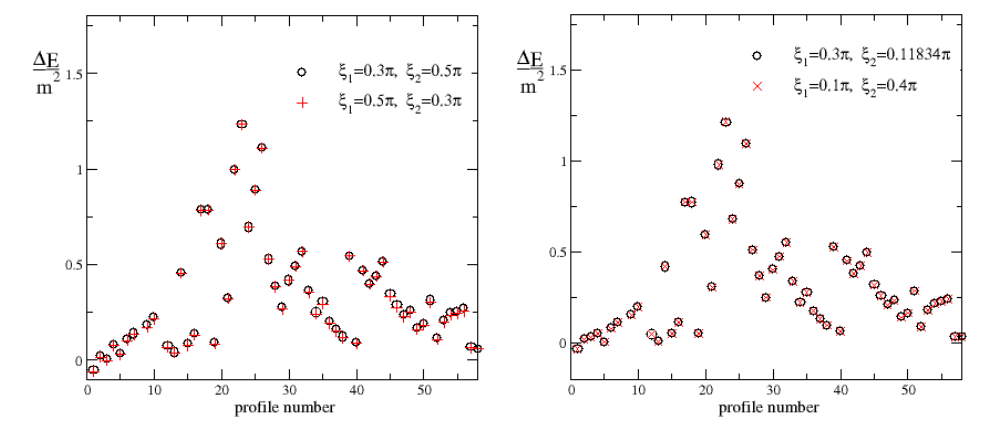


Fig. 4. The vacuum polarization energy for different background profiles for two sets of angles. Each set has the same product s_1s_2 . The profile counting on the horizontal axis goes by different values of the width parameters w_G and w_H .

dozen profile functions characterized by different w_G and w_H . Of course, swapping the two angles would not change the VPE if it were a function of their sum. We therefore also present in the right panel of Fig. 4 the results from an alternative set of angles with identical s_1s_2 . Reference 64 verifies the isospin invariance for more sets of angles. With the confirmation of this invariance, we conclude that ξ_2 is a redundant variational parameter and we may without loss of generality simplify to the case of $\xi_2 = \frac{\pi}{2}$, for which the Dirac Hamiltonian has real matrix elements.

4.4.3. Stable charged strings

Although the VPE alone does not stabilize classical string configurations, strings with fermion charge can potentially be stabilized by having lower energy than the same number of free fermions. Wide strings in particular generate many fermion bound states. Their energy eigenvalues are of the same order in the semi-classical \hbar expansion as the VPE, however, so the inclusion of these levels ultimately requires consideration of the VPE as well.

We want to compute the binding energy per unit length for a prescribed charge per unit length Q. Let $0 < \omega_i \le m$ be a bound state eigenvalue of the Dirac Hamiltonian whose interaction part is given in Eq. (51). Then a state has energy $[\omega_i^2 + p^2]^{1/2}$, where p is the conserved momentum along the symmetry axis. To count the populated states, we introduce a chemical potential μ such that $\min\{\omega_i\} \leq \mu \leq m$. States with $[\omega_i^2 + p^2]^{1/2} < \mu$ are filled while states with $[\omega_i^2 + p^2]^{1/2} > \mu$ remain empty. For each bound state, this defines the Fermi momentum $P_i(\mu) = [\mu^2 - \omega_i^2]^{1/2}$, and the charge (per unit length) is

$$Q(\mu) = \sum_{\omega_i \le \mu} \int_{-P_i(\mu)}^{P_i(\mu)} \frac{dp}{2\pi} = \frac{1}{\pi} \sum_{\omega_i \le \mu} P_i(\mu).$$
 (75)

The sum runs over all bound states available for a given chemical potential. This relation can be inverted to give $\mu = \mu(Q)$: For prescribed Q, we increase μ from $\min\{\omega_i\}$ until the right-hand side of Eq. (75) matches. The same number of noninteracting fermions has energy of at least Qm, giving the binding energy^c per unit length

$$E_{\rm b}(Q) = E_{\rm cl} + N\Delta E + \frac{N}{\pi} \sum_{i} \int_{0}^{P_i(\mu(Q))} dp \left[\sqrt{\omega_i^2 + p^2} - m \right].$$
 (76)

For a prescribed charge Q, we find an upper bound on $E_b(Q)$ by scanning several hundred configurations, parameterized by different values of w_H , w_G and ξ_1 .

This model is similar to the Standard Model of particle physics and we thus adopt the parameters from Eq. (47) together with N=3 (for color). Eventually we will allow for a heavy (fourth) generation of fermions and thus vary the Yukawa coupling f.

The left panel of Fig. 5 shows the fermion contribution to the energy $E_{\rm b}$ as a function of the charge. As mentioned in Subsec. 4.4.1, for wide profiles there is only very mild dependence on ξ_1 and the specific value is not essential. Those graphs terminate at the charge when all bound states are occupied. The energy $E_{\rm b}$ is smaller the wider the string configuration because the number of available bound states increases with the width, in particular with the width of the scalar component of the Higgs field.

The right panel of Fig. 5 gives the final result for the binding energy. When measured in units of the fermion mass m^2 , the fermion contribution does not scale with the Yukawa coupling f while the Higgs contribution to the classical energy, Eq. (48), scales like $\frac{1}{f^2}$. Hence for a large enough coupling constant, $E_{\rm b}$ will dominate. From that figure we find that the critical value above which binding is observed is about $f_{\rm c} \approx 1.7$, corresponding to a fermion with mass of approximately 300 MeV. The larger the Yukawa coupling, the smaller the charge of the bound configuration.

We have not included the interaction among the fermions that build the charge. This is similar to the description of atomic levels from the hydrogen spectrum. Also, the full back-reaction on the meson profiles is not included. However, we stress that

^cHere, we define the binding energy such that a negative value indicates binding.

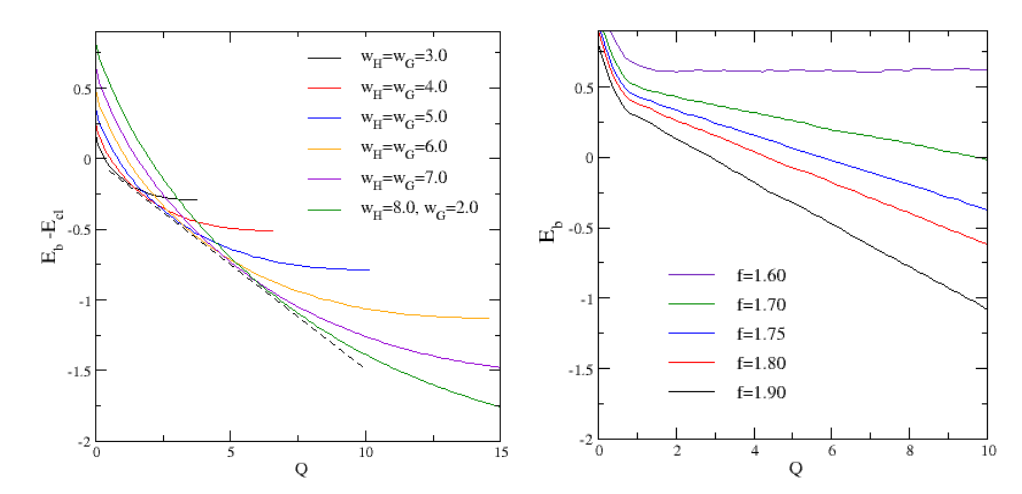


Fig. 5. For the model parameters of Eq. (47) the left panel shows the fermion energy when Q levels are occupied for selected variational parameters at $\xi_1 = 0.4\pi$. The optimal value follows a straight line (dashed). The right panel gives the optimal binding energy as function of the charge for several Yukawa constants. All other model parameters are from Eq. (47).

since we are using a variational approach, such a modification can only lower the total energy.

5. Vortices

In this section, we compute the VPE of Abrikosov–Nielsen–Olesen (ANO) vortices^{65–67} for different topological charges. There are multiple applications of such vortices in physics: In condensed matter physics, the dependence of the energy on the topological charge is essential for distinguishing superconductors of type I, where the energy increases weaker than linearly with charge and multiple vortices coalesce, from type II, where energy increases stronger than linearly and single, isolated vortices emerge. In particle physics applications the topological charge is often identified as the particle number; therefore these studies provide important insight for binding energies beyond the classical level.

These vortices consist of a scalar Higgs field with spontaneous symmetry breaking and an Abelian gauge field. For simplicity we consider the BPS case with equal masses, which classically represents the transition between type I and type II superconductors.

5.1. Classical fields

Classical vortices are constructed from the Lagrangian of scalar electrodynamics with spontaneous symmetry breaking

$$\mathcal{L} = -\frac{1}{4}F_{\mu\nu}F^{\mu\nu} + |D_{\mu}\Phi|^2 - \frac{\lambda}{4}(|\Phi|^2 - v^2)^2, \tag{77}$$

where $F_{\mu\nu} = \partial_{\mu}A_{\mu} - \partial_{\nu}A_{\mu}$ is the field strength tensor and $D_{\mu}\Phi = (\partial_{\mu} - ieA_{\mu})\Phi$ is the covariant derivative of the complex Higgs field.

We will need to consider fluctuations about vortex backgrounds that approach free cylindrical waves as $\rho \to \infty$. This requires the so-called singular gauge, which is characterized by two profile functions h and q in

$$\Phi_S = vh(\rho) \quad \text{and} \quad \mathbf{A}_S = nv\hat{\boldsymbol{\varphi}} \frac{g(\rho)}{\rho},$$
(78)

where $\rho = evr$ is dimensionless while r is the physical distance from the vortex, and furthermore $\hat{\varphi}$ is the azimuthal unit vector for the vortex axis. The temporal and longitudinal components of the gauge field vanish classically, $A_S^0 = A_S^3 = 0$. The winding number n is the essential topological quantity. In the BPS case with $\lambda = 2e^2$, the energy functional is minimized when the profile functions obey the first-order differential equations

$$g' = \frac{\rho}{n}(h^2 - 1)$$
 and $h' = \frac{n}{\rho}gh$, (79)

with the singular gauge boundary conditions

$$h(0) = 1 - g(0) = 0$$
 and $\lim_{\rho \to \infty} h(\rho) = 1 - \lim_{\rho \to \infty} g(\rho) = 1.$ (80)

The resulting energy per unit length is linear in the winding number, $E_{\rm cl} = 2\pi n v^2$. The differential equations (79) can be solved numerically, but for later use in the scattering problem an approximate expression in terms of elementary functions is very helpful. It turns out that for $1 \le n \le 4$ the correlation coefficients for the fit

$$h(\rho) = \alpha_2 \tanh^n(\alpha_1 \rho) + [1 - \alpha_2] \tanh^n(\alpha_0 \rho),$$

$$g(\rho) = \beta_1 \rho \frac{1 - \tanh^2(\beta_2 \rho)}{\tanh(\beta_1 \rho)},$$

with the fit parameters α_i and β_i listed in Table 4 deviate from unity by 10^{-4} or less from the numerical solutions to Eq. (79).

5.2. Quantum theory

To quantize the theory, we introduce fluctuations about the vortex via

$$\Phi = \Phi_S + \eta \quad \text{and} \quad A^{\mu} = A_S^{\mu} + a^{\mu} \tag{81}$$

Table 4. Fit parameters for vortex profiles.

\overline{n}	α_0	α_1	α_2	β_1	β_2
1	0.8980	0.6621	0.1890	0.5361	0.7689
2	0.9072	0.8288	2.6479	1.0949	0.8042
3	0.8290	0.7882	5.1953	1.1328	0.7425
4	0.7755	0.7350	5.2009	1.1034	0.6853

and extract the harmonic terms in the fluctuations η and a^{μ} . Their gauge is fixed by adding an R_{ξ} type Lagrangian that cancels the $\eta \partial_{\mu} a^{\mu}$ and $\eta^* \partial_{\mu} a^{\mu}$ terms

$$\mathcal{L}_{gf} = -\frac{1}{2}G^2 = -\frac{1}{2}[\partial_{\mu}a^{\mu} + ie(\Phi_S \eta^* - \Phi_S^* \eta)]^2.$$
 (82)

We still have to account for the ghost contribution to the VPE associated with this gauge fixing. The infinitesimal gauge transformations read

$$A^{\mu} \to A^{\mu} + \partial^{\mu} \chi, \quad \Phi_S + \eta \to \Phi_S + \eta + ie\chi(\Phi_S + \eta)$$
 (83)

so that $a^{\mu} \to a^{\mu} + \partial^{\mu} \chi$ and $\eta \to \eta + ie\chi(\Phi_S + \eta)$. Then

$$\left. \frac{\partial G}{\partial \chi} \right|_{\chi=0} = \partial_{\mu} \partial^{\mu} + e^2 (2|\Phi_S|^2 + \Phi_S \eta^* + \Phi_S^* \eta) \tag{84}$$

induces the ghost Lagrangian^{68,69}

$$\mathcal{L}_{gh} = \overline{c}(\partial_{\mu}\partial^{\mu} + 2e^{2}|\Phi_{S}|^{2})c + \text{nonharmonic terms.}$$
 (85)

The corresponding VPE is that of a Klein–Gordon field with mass $\sqrt{2}ev$ in the background potential $2(|\Phi_S|^2 - v^2) = 2v^2(h^2 - 1)$, which must be multiplied by a factor of negative two, corresponding to a complex scalar ghost field, and combined with the VPE obtained for the gauge and scalar fields. Since $D_0\Phi_S = 0$ and $D_3\Phi_S = 0$, the temporal and longitudinal components a^0 and a^3 fully decouple, contributing

$$-\frac{1}{2}[\partial_{\mu}a_{0}\partial^{\mu}a^{0}+\partial_{\mu}a_{3}\partial^{\mu}a^{3}]+|\Phi_{S}|^{2}[a_{0}a^{0}+a_{3}a^{3}]$$

to the Lagrangian. These fluctuations are both subject solely to the background potential $2(|\Phi_S|^2 - v^2)$, which is exactly the same as that of the ghosts. As a result, the nontransverse and ghost contributions to the VPE cancel each other. Of course, this just reflects the fact that the free electromagnetic field only has two physical degrees of freedom. Thus, we end up with the truncated Lagrangian for the relevant quantum fluctuations

$$\mathcal{L}^{(2)} = \frac{1}{2} \sum_{n=1,2} (\partial_{\mu} a_n) (\partial^{\mu} a_n) - e^2 |\Phi_S|^2 \sum_{n=1,2} a_n^2 + |\dot{\eta}|^2 - |\partial_3 \eta|^2 + \sum_{n=1,2} (D_n \eta)^* (D^n \eta) - e^2 [3|\Phi_S|^2 - v^2] |\eta|^2 + 2ie \sum_{n=1,2} a_n [\eta^* (D^n \Phi_S) - \eta (D^n \Phi_S)^*].$$
(86)

Essentially we have simplified the theory to that of four real scalar fields: a_1 , a_2 , $Re(\eta)$ and $Im(\eta)$.

To formulate the scattering problem, we employ a partial wave decomposition using the complex combinations in units with ev = 1 (resulting in mass parameters $M_H = M_A = \sqrt{2}$),

$$a^{1} + ia^{2} = \sqrt{2}ie^{-i\omega t} \sum_{\ell} a_{\ell}(\rho)e^{i\ell\varphi}$$
 and $\eta = e^{-i\omega t} \sum_{\ell} \eta_{\ell}(\rho)e^{i\ell\varphi}$, (87)

leading to a 4×4 scattering problem for the radial functions. For profile functions obeying Eq. (79), this problem decouples into two 2×2 systems, with the one for a^* and η^* being the same as that of a and η . Hence it suffices to compute the VPE of the latter and double it. The scattering problem is set up in terms of the Jost solution \mathcal{F}_{ℓ} by introducing

$$\begin{pmatrix} \eta_{\ell}^{(1)} & \eta_{\ell}^{(2)} \\ a_{\ell+1}^{(1)} & a_{\ell+1}^{(2)} \end{pmatrix} = \mathcal{F}_{\ell} \cdot \mathcal{H}_{\ell} \quad \text{where } \mathcal{H}_{\ell} = \begin{pmatrix} H_{\ell}^{(1)}(q\rho) & 0 \\ 0 & H_{\ell+1}^{(1)}(q\rho) \end{pmatrix}. \tag{88}$$

The superscripts on the left-hand side refer to the two possible scattering channels when imposing the boundary condition $\lim_{\rho\to\infty} \mathcal{F}_\ell = 1$. The Hankel functions $H_\ell^{(1)}$ parameterize outgoing cylindrical waves. In matrix form, the scattering differential equation in terms of the dimensionless imaginary momentum $t = i\sqrt{\omega^2 - 2}$ reads

$$\frac{\partial^2}{\partial \rho^2} \mathcal{F}_{\ell} = -\frac{\partial}{\partial \rho} \mathcal{F}_{\ell} - 2\left(\frac{\partial}{\partial \rho} \mathcal{F}_{\ell}\right) \cdot \mathcal{Z}_{\ell} + \frac{1}{\rho^2} [\mathcal{L}_{\ell}, \mathcal{F}_{\ell}] + \mathcal{V}_{\ell} \cdot \mathcal{F}_{\ell}, \tag{89}$$

where angular momenta enter via the derivative matrix for the analytically continued Hankel functions

$$\mathcal{Z}_{\ell} = \begin{pmatrix} \frac{|l|}{\rho} - t \frac{K_{|l|+1}(t\rho)}{K_{|l|}(t\rho)} & 0 \\ 0 & \frac{|l+1|}{\rho} - t \frac{K_{|l+1|+1}(t\rho)}{K_{|l+1|}(t\rho)} \end{pmatrix} \text{ and } \mathcal{L}_{\ell} = \begin{pmatrix} \ell^{2} & 0 \\ 0 & (\ell+1)^{2} \end{pmatrix}. \tag{90}$$

The potential matrix is

$$\mathcal{V}_{\ell} = \begin{pmatrix} 3(h^{2}(\rho) - 1) + \frac{n^{2}g^{2}(\rho) - 2n\ell g(\rho)}{\rho^{2}} & \sqrt{2}d(\rho) \\ \sqrt{2}d(\rho) & 2(h^{2}(\rho) - 1) \end{pmatrix}, \tag{91}$$

with $d(\rho) = \frac{dh(\rho)}{d\rho} + \frac{n}{\rho}h(\rho)g(\rho)$. We then use Eq. (89) to compute the Jost function, which is given by $\nu_{\ell}(t) = \lim_{\rho \to 0} \ln \det[\mathcal{F}_{\ell}]$.

5.3. Removal of gauge-variant divergence

The Higgs-Higgs component of the potential matrix in Eq. (91) diverges like $\frac{1}{\rho^2}$ as $\rho \to 0$. This singular behavior has neither well-defined Born nor Feynman series. Hence we need to develop an alternative method to handle the associated ultraviolet divergences. To study these divergences in more detail, we display all divergent one-loop diagrams arising from Higgs fluctuations in Figs. 6–8. Figure 6 shows the Feynman diagrams that superficially are quadratically divergent. Due to gauge invariance, the quadratic divergences of 6(a) and 6(b) cancel. Diagram 6(d) is a total derivative and vanishes (with a translationally invariant regularization). Indeed all diagrams with an odd number of gauge field insertions are finite because of Lorentz

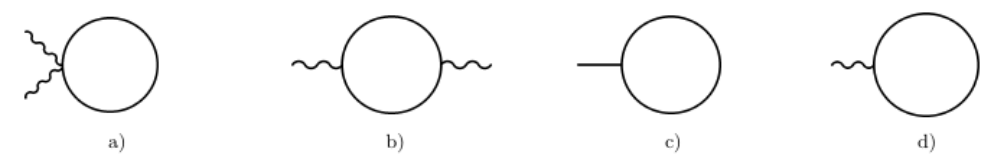


Fig. 6. Quadratically divergent one-loop diagrams with a Higgs field in the loop. External lines represent (Fourier transforms of) the classical Higgs (straight) and gauge (curly) fields.

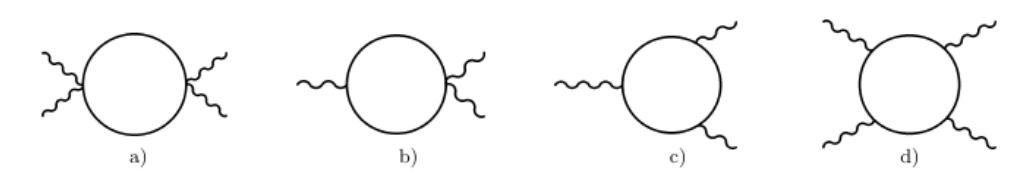


Fig. 7. Logarithmically divergent one-loop Higgs diagrams with external photon lines only.

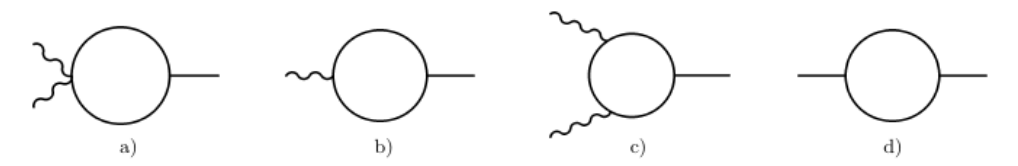


Fig. 8. Logarithmically divergent one-loop Higgs diagrams with at least one insertion of the Higgs potential $V_H = 3(h^2 - 1)$.

invariance and the fact that $\partial_{\mu}A_{S}^{\mu}=0$. Hence the only remaining quadratic divergence is the tadpole graph with a single insertion of $V_{H}=3(h^{2}(\rho)-1)$, as shown in 6(c). This diagram is local, meaning it is independent of the incoming momentum and thus proportional to $\int d^{2}xV_{H}$, so it can be fully removed from the VPE by an appropriate no-tadpole renormalization condition. Again by gauge invariance, the logarithmic divergences in 7(a) and 7(d) cancel, as do those of 8(a) and 8(c). Thus all we need to consider are the divergences associated with the diagrams of Figs. 6(a)–6(c) and 8(d). The treatment of 6(c) and 8(d) is straightforward using the methods we have discussed above, but additional subtleties arise for 6(a) and 6(b).

When restricting to Higgs fluctuations in the loop, these methods require analysis of a single second-order differential equation for the factor function of the Jost solution

$$\frac{1}{\rho}\partial_{\rho}\rho\partial_{\rho}\overline{\eta}_{\ell} = 2tZ_{\ell}(t\rho)\partial_{\rho}\overline{\eta}_{\ell} + \frac{1}{\rho^{2}}[g^{2}(\rho) - 2\ell g(\rho)]\overline{\eta}_{\ell} + V_{H}(\rho)\overline{\eta}_{\ell}$$
(92)

with $Z_{\ell}(z) = \frac{K_{|\ell|+1}(z)}{K_{|\ell|}(z)} - \frac{|\ell|}{z}$. Let $\overline{\eta}_{\ell}^{(1,2)}$ be the solutions for $\overline{\eta}_{\ell}$ at first- and second-order in $V_H(\rho)$, but zeroth order in the gauge field. Thus $\overline{\eta}_{\ell}^{(1,2)}$ relate to the diagrams 6(c) and 8(d). The scattering data analog of diagram 6(a) is governed by the

differential equation

$$\frac{1}{\rho}\partial_{\rho}\rho\partial_{\rho}\overline{\eta}_{\ell}^{(3)} = 2tZ_{\ell}(t\rho)\partial_{\rho}\overline{\eta}_{\ell}^{(3)} + \left(\frac{g(\rho)}{\rho}\right)^{2},\tag{93}$$

while diagram 6(b) is associated with a set of coupled differential equations

$$\frac{1}{\rho}\partial_{\rho}\rho\partial_{\rho}\overline{\eta}_{\ell}^{(4)} = 2tZ_{\ell}(t\rho)\partial_{\rho}\overline{\eta}_{\ell}^{(4)} - \frac{2\ell}{\rho^{2}}g(\rho),$$

$$\frac{1}{\rho}\partial_{\rho}\rho\partial_{\rho}\overline{\eta}_{\ell}^{(5)} = 2tZ_{\ell}(t\rho)\partial_{\rho}\overline{\eta}_{\ell}^{(5)} - \frac{2\ell}{\rho^{2}}g(\rho)\overline{\eta}_{\ell}^{(4)}.$$
(94)

The boundary conditions are such that $\overline{\eta}_{\ell} \to 1$ while all $\overline{\eta}_{\ell}^{(i)} \to 0$ as $\rho \to \infty$. Numerical simulations⁴⁵ for regular profiles, i.e. Eq. (80) replaced by $g(\rho) \sim 0$ at the center of the vortex, verify that for sufficiently large t

$$\sum_{\ell=-\infty}^{\infty} \lim_{\rho \to 0} \left\{ \ln(\overline{\eta}_{\ell}) - \overline{\eta}_{\ell}^{(1)} - \overline{\eta}_{\ell}^{(2)} + \frac{1}{2} (\overline{\eta}_{\ell}^{(1)})^{2} - \overline{\eta}_{\ell}^{(3)} - \overline{\eta}_{\ell}^{(4)} - \overline{\eta}_{\ell}^{(5)} + \frac{1}{2} (\overline{\eta}_{\ell}^{(4)})^{2} \right\} \propto \frac{1}{t^{4}}.$$
(95)

This guarantees a finite integral in Eq. (21). More surprisingly, those numerical experiments also verify that

$$\sum_{\ell=-\infty}^{\infty} \lim_{\rho \to 0} \left\{ \overline{\eta}_{\ell}^{(3)} + \overline{\eta}_{\ell}^{(4)} + \overline{\eta}_{\ell}^{(5)} - \frac{1}{2} (\overline{\eta}_{\ell}^{(4)})^2 \right\} \longrightarrow n^2 \int_0^{\infty} \frac{d\rho}{\rho} g^2(\rho) \quad \text{as } t \to \infty, \quad (96)$$

signaling a quadratic divergence. It is exactly the quadratic divergence that would emerge from diagrams 6(a) and 6(b) if the loop were not regularized in a gauge-invariant manner. A gauge invariant treatment, however, should lead to only a logarithmic divergence, reflected by an asymptotic $\frac{1}{t^2}$ behavior. We recall that Eq. (21) originated from integrating $\frac{d[\nu(t)]_N}{dt}$ by parts after the analytic continuation of Eq. (20). Hence the subtraction of the integral in Eq. (96) from $[\nu(t)]$ does not alter the VPE, but rather it restores gauge invariance of the expression in Eq. (21).

Unfortunately, the integral in Eq. (96) does not exist for the singular vortex profile. Similarly the (first-order) Born approximation does not exist. However, we may consider

$$[\nu(t)]_{H} = \lim_{L \to \infty} \sum_{\ell=-L}^{L} \left\{ \ln(\overline{\eta}_{\ell}) - \overline{\eta}_{\ell}^{(1)} - \overline{\eta}_{\ell}^{(2)} + \frac{1}{2} (\overline{\eta}_{\ell}^{(1)})^{2} \right\} \bigg|_{\rho=\rho_{\min}} - n^{2} \int_{\rho_{\min}}^{\infty} \frac{d\rho}{\rho} g^{2}(\rho),$$
(97)

which subtracts the gauge invariant logarithmic divergence of diagrams 6(a) and 6(b) when $\rho_{\min} \to 0$, even for singular backgrounds. On the left hand side the H subscript denotes the V_H subtraction at linear and quadratic orders. The numerical simulations confirm that indeed $[\nu(t)]_H$ does not diverge in that limit.

Using dimensional regularization $(D = 4 - 2\epsilon)$ the logarithmic divergence in the combination of diagrams 6(a) and 6(b) is

$$E^{(A)}|_{\text{div.}} = \frac{1}{12\epsilon(4\pi)^2} \int d^2x \, F_{\mu\nu} F^{\mu\nu} = \frac{1}{96\pi^2} \left[\int d^2x \, F_{\mu\nu} F^{\mu\nu} \right] \int_0 \frac{l^2 dl}{\sqrt{l^2 + M^2}} \bigg|_{\text{div.}}$$
(98)

Hence we expect that

$$\lim_{\rho_{\min} \to 0} [\nu(t)]_H \longrightarrow \nu_{\text{l.f.}}(t) = \frac{1}{t^2} \frac{n^2}{12} \int_0^\infty \rho \, d\rho \left(\frac{g'(\rho)}{\rho}\right)^2 \quad \text{as } t \to \infty.$$
 (99)

To simplify the simulation we employ a one-parameter (α) set of trial profile functions

$$h(\rho) = \tanh(\alpha \rho)$$
 and $g(\rho) = e^{-(\alpha \rho)^2}$ (100)

that reflect the singular structure of the vortex appropriately. Numerically we cannot take the angular momentum sum in Eq. (97) to infinity. Rather we consider $\nu_L(t)$ as the $\rho_{\min} \to 0$ limit of the right-hand side evaluated with finite limits $(-L,\ldots,+L)$ on the sum. In order to reach the asymptotic behavior, these limits must increase with the (imaginary) momentum t. In the left panel of Fig. 9, we display $\nu_L(t)$ for values as large as L=500. This graph indeed suggests convergence of the angular momentum sum for moderate values of t. However, there are at least two problems. First, the asymptotic value seems to be negative, while $\nu_{\text{l.f.}}(t)>0$. Second, $\nu_L(t)$ approaches zero approximately like $\frac{1}{t^4}$, as the middle panel of Fig. 9 suggests. If correct, it would imply that the integral $\int_{-\infty}^{\infty} dt \, \nu_L(t)$ is finite^d and that the counterterm for the logarithmic divergence from the diagrams 6(a) and 6(b) would not be compensated. It turns out that for momenta as small as $t\approx 6$, $\nu_{500}(t)$ has not reached the asymptotic value, as clearly seen in the right panel of Fig. 9. Numerically L>600 is difficult to handle and costly in CPU-time because of the

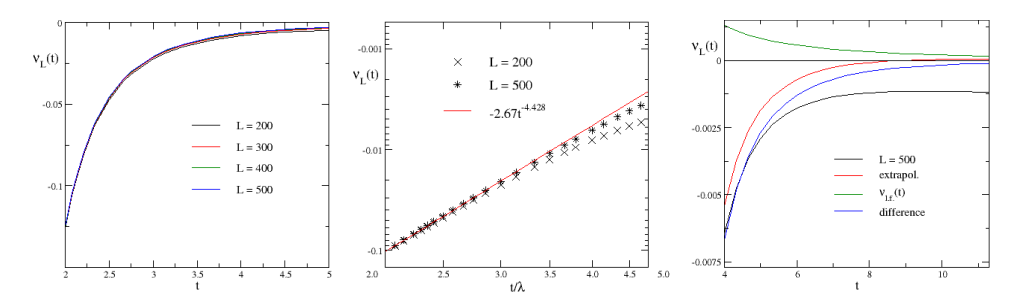


Fig. 9. Asymptotic behavior of $\nu_L(t)$ for $\alpha = 0.5$ in Eq. (100) and n = 1. Left panel: different maximal angular momenta L; center panel: fit showing that $\nu_L(t)$ falls faster than $1/t^2$ for moderate values of t; right panel: extrapolation $L \to \infty$ and limiting function from Eq. (99).

^dThis has caused confusion in earlier publications, cf. Refs. 70 and 59.

singular behavior of the modified Bessel functions at small arguments. Instead an extrapolation from $L \in [300, 600]$ to infinity is required. Indeed, that infinite L extrapolation turns positive at large t and the difference from $\nu_{\text{l.f.}}(t)$ is numerically confirmed to decay faster than $\frac{1}{t^3}$. The results shown in Fig. 9 are for topological charge n=1, but the cases n=2,3,4 have been confirmed to follow the same behavior.

We have thus shown that both the subtraction of the constant in Eq. (99) and the extrapolation to infinite angular momentum are necessary to comply with gauge invariance.

5.4. VPE for different topological charges

We want to adopt the procedure established above to the VPE of the ANO vortex, with $\nu_{\ell}(t) = \lim_{\rho \to 0} \ln \det[\mathcal{F}_{\ell}]$ where \mathcal{F}_{ℓ} is matrix solution to Eq. (89). Since we must separate the singular terms of the Higgs-Higgs component of the potential matrix, we introduce

$$\overline{\mathcal{V}} = \begin{pmatrix} 3(h^2(\rho) - 1) & \sqrt{2}d(\rho) \\ \sqrt{2}d(\rho) & 2(h^2(\rho) - 1) \end{pmatrix}$$
 (101)

and let $\overline{\nu}_{\ell}^{(1)}$ and $\overline{\nu}_{\ell}^{(2)}$ be the first two Born terms originating from $\overline{\mathcal{V}}$. They are the scattering data analog of the diagrams 6(c), 8(d) and those in Fig. 10. The above analysis suggests that^e

$$[\nu(t)]_{V} = \lim_{\substack{L \to \infty \\ \rho_{\min} \to 0}} \left\{ \sum_{\ell=-L}^{L} \left[\nu_{\ell}(t) - \overline{\nu}_{\ell}^{(1)}(t) - \overline{\nu}_{\ell}^{(2)}(t) \right]_{\rho_{\min}} - n^{2} \int_{\rho_{\min}}^{\infty} \frac{d\rho}{\rho} g^{2}(\rho) \right\}$$
(102)

approaches $\frac{n^2}{12t^2} \int_0^\infty \rho \, d\rho (\frac{g'(\rho)}{\rho})^2$ as $t \to \infty$. We treat the resulting logarithmic divergence using the fake boson method introduced in Subsec. 2.5. Then the scattering part of the VPE reads

$$\Delta E_{\text{scat.}} = \frac{1}{2\pi} \int_{\sqrt{2}}^{\infty} t dt \left[[\nu(t)]_V - C_B \nu_B^{(2)}(t) \right], \tag{103}$$

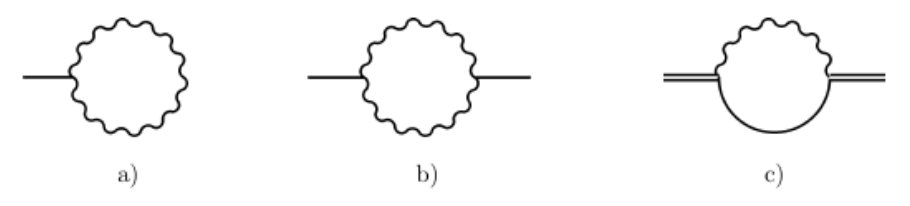


Fig. 10. Additional divergent one-loop diagrams in the presence of gauge fluctuations. The double line indicates the insertion of the off-diagonal interaction $d(\rho)$.

^eIn the numerical analysis an extrapolation as in Eq. (69) is needed for channels with $|\ell| \le n$. This minor (\sim 1%) correction was not included in Ref. 71.

and for the choice $V_B(\rho) = 3(\tanh^2(\zeta \rho) - 1)$ the fake boson coefficient becomes

$$C_B = -\frac{n^2}{3} \frac{\int_0^\infty \rho d\rho (\frac{g'(\rho)}{\rho})^2}{\int_0^\infty \rho d\rho [3(\tanh^2(\zeta\rho) - 1)]^2}.$$
 (104)

Here ζ is a tunable parameter that has no effect once the renormalized Feynman diagram, which is obtained from two insertions of V_B and subsequent multiplication by C_B , is added.

The counterterm Lagrangian reads

$$\mathcal{L}_{CT} = c_1 F_{\mu\nu} F^{\mu\nu} + c_2 |D_{\mu}\Phi|^2 - c_3 (|\Phi|^2 - v^2)^2 - c_4 (|\Phi|^2 - v^2). \tag{105}$$

The first three terms are from the original Lagrangian, Eq. (77). The last term cancels the tadpole diagrams and is generated from the original Lagrangian by varying the vacuum expectation value v. Hence the no-tadpole condition fixes c_4 and ensures that v has no quantum corrections. As in Subsec. 4.4, we impose on-shell conditions to fix the counterterm coefficients c_1 , c_2 , and c_3 . This requires consideration of the diagrams 6(a), 6(b), 8(d) as well as 10(b) and 10(c). For example, in momentum space the diagrams 6(a) and 6(b) yield the dimensionally regularized action (returning to physical units with $M = \sqrt{2}ev$)

$$\Gamma \bigg(1 - \frac{D}{2}\bigg) \left(\frac{eM}{4\pi}\right)^2 \left(\frac{4\pi\mu^2}{M^2}\right)^{2 - \frac{D}{2}} \int \frac{d^4p}{(2\pi)^4} \, \widetilde{A}_{\mu}(p) \widetilde{A}^{\mu}(-p) \int_0^1 dx [1 - X(x,p)^{\frac{D}{2} - 1}],$$

where $X(x,p) = 1 - x(1-x)\frac{p^2}{M^2}$. By gauge invariance the residue at D=2 vanishes and we can analytically continue to $D=4-2\epsilon$ with the renormalization scale μ^2

$$-\frac{e^{2}}{96\pi^{2}} \left[\frac{1}{\epsilon} + 1 - \gamma + \ln \frac{4\pi\mu^{2}}{M^{2}} \right] \int \frac{d^{4}p}{(2\pi)^{4}} p^{2} \widetilde{A}_{\mu}(p) \widetilde{A}^{\mu}(-p)$$

$$+ \left(\frac{eM}{4\pi} \right)^{2} \int \frac{d^{4}p}{(2\pi)^{4}} \widetilde{A}_{\mu}(p) \widetilde{A}^{\mu}(-p) \int_{0}^{1} dx \, X(x,p) \ln[X(x,p)].$$

Combining this result with the first term in Eq. (105) and separating the divergent part of the counterterm coefficient via $2c_1 = \frac{e^2}{96\pi^2} \left[\frac{1}{\epsilon} + 1 - \gamma + \ln \frac{4\pi\mu^2}{M^2}\right] + c_A$ yields^f

$$\int \frac{d^4p}{(2\pi)^4} p^2 \widetilde{A}_{\mu}(p) \widetilde{A}^{\mu}(-p) G_A(p^2),$$

where

$$G_A(p^2) = c_A + \left(\frac{eM}{4\pi}\right)^2 \frac{1}{p^2} \int_0^1 dx \, X(x,p) \ln[X(x,p)].$$

Quantum corrections are eliminated from the residue of the gauge field propagator by setting $G_A(M^2) = 0$, which determines c_A . The condition on the residue of the Higgs propagator determines c_2 from diagram 10(c), while the combination of the

^fNote that for the vortex $\partial_{\mu}A_{S}^{\mu}=0$ and thus $p_{\mu}\widetilde{A}^{\mu}(p)=0$. Also note that $\ln[X(x,0)]=0$ so that $G_{A}(p^{2})$ is regular when $p^{2}\to 0$.

Table 5. VPE of ANO vortices with different topological charges. The parameters in the fake boson potential are $\zeta = 1, 0.9, 0.8, 0.7$ for n = 1, 2, 3, 4, respectively.

	n = 1	n = 2	n = 3	n=4
$\Delta E_{\rm scat.}$	-0.0510	-0.1937	-0.3563	-0.5251
$E_{\mathrm{FD}}^{\mathrm{ren.}}$	0.0448	0.0558	0.0840	0.1171
ΔE	-0.0063	-0.1379	-0.2722	-0.4080

diagrams 6(c) and 10(b) yields c_3 by demanding that the Higgs mass is not changed by quantum effects. It is worth noting that the equality of Higgs and gauge field masses is maintained when one-loop quantum corrections are included.

With all counterterm coefficients determined, we can write the (renormalized) Feynman diagram piece of the VPE as

$$E_{\rm FD}^{\rm ren.} = C_B E_{\rm FD}^{(2)} + E_{\rm FD}^{(0)} + E_{\rm CT}.$$
 (106)

The Feynman diagram with two insertions of V_B gives $E_{\rm FD}^{(2)}$, while $E_{\rm FD}^{(0)}$ originates from diagrams 6(c), 8(d), 10(b) and 10(c). By construction, $C_B E_{\rm FD}^{(2)}$ has the same ultra-violet divergence as the combination of the diagrams 6(a) and 6(b). Hence all such divergences cancel in $E_{\rm FD}^{\rm ren}$.

We list the numerical results in Table 5. We have also performed simulations with different values for ζ and ensured equal results for ΔE to the given precision. (Of course, the individual contributions $E_{\rm FD}^{\rm ren.}$ and $\Delta E_{\rm scat.}$ vary with ζ .) We observe a constant increment of ΔE with the topological charge. More precisely, the fit $\Delta E(n) = -0.005 - 0.134(n-1)$ has very small $\chi^2 = 4.5 \times 10^{-6}$. Since the classical energy is linear in n for the case of equal Higgs and gauge field masses, the total binding energy, $E_{\rm rel} = \Delta E(n) - n\Delta E(1) = -0.129(n-1)$, is negative. This suggests that these vortices coalesce.

Though this is the first computation of the VPE for soliton-like configurations with different topological charges in a renormalizable theory, it is merely the beginning for computing the VPE of vortices. The case with two space dimensions will be next step. Subsequently the case of different Higgs and gauge field masses should also be considered.

6. Summary

In this short review, we have reported recent progress on the computation of vacuum polarization energies (VPE) of soliton-like structures in renormalizable quantum field theories using spectral methods. For earlier applications of these methods we refer to the lecture notes of Ref. 8.

For static background configurations like solitons, quantum fluctuations obey wave equations analogous to those in ordinary quantum mechanics, with a potential induced by the soliton. Spectral methods then determine the bound state energies and scattering data (S-matrix, phase shifts) for that potential. Formally these data

yield the VPE as a sum of the bound state energies and a momentum integral over the phase shift, but it is a subtle problem to unambiguously combine the ultraviolet divergences with the counterterms of the quantum theory. These counterterm coefficients are universal for a prescribed set of renormalization conditions and not sensitive to the particular soliton configuration. This problem is solved by the observation that there are two equivalent expansions for the VPE in powers of the background potential: (i) the sum of Feynman diagrams in the quantum field theory and (ii) the Born series for scattering data. In both cases, the series expansion approaches the ultra-violet behavior of the full result. To implement the renormalization procedure, the relevant Born terms are then subtracted from the integrand of the momentum integral and added back in form of the equivalent Feynman diagrams, which are then unambiguously combined with the counterterms using standard techniques.

Here we have focused on the use of the analytic properties of the scattering data, represented by the Jost function, to evaluate the momentum integral along the imaginary momentum axis. This approach has, among others, the advantage that the bound state energies need not be explicitly computed. We have shown that for popular soliton models in one dimension this approach allows one to compute the VPE very efficiently. Moreover, with an appropriate treatment of the mass gap when analytically continuing, the VPE for soliton models with quantum fluctuations with different masses can be evaluated as well. We stress that the Jost function is not computed in any approximation and that its Born expansion solely serves to identify the ultra-violet divergences from the quantum field theory in the scattering data.

These enhanced spectral methods have made possible the computation of the VPE of more intricate configurations in particular quantum field theories. In turn, these studies lead to a number of interesting and novel observations:

- In models with one space dimension we have documented the novel effect of quantum destabilization of solitons. The conjecture is that in theories with multiple (distinct) vacua in field space that have different curvatures of the field potential, the soliton may approximately assume either of these vacuum configurations in separated regions. As the sizes of these regions vary, the VPE, and, as a result, the total energy, may decrease without a lower bound. We have demonstrated this scenario explicitly for the Shifman–Voloshin soliton, which has two field components with different masses. Models with field potentials of higher polynomial order also support this conjecture, though there the situation is less stringent because the two separated regions both extend to spatial infinity (positive and negative).
- We have also expressed the interface formalism, which was first developed to
 describe domain walls or surfaces subject to the Casimir force, in terms of imaginary momentum integrals. This approach made possible the computation of the
 energy carried by fermions in the background of cosmic strings. At the center of

the string, the gauge field has singularities. Fortunately, for nonabelian strings the fields are single-valued and the singularity can be removed by a local gauge transformation. Neither the components of the Born series nor individual Feynman diagrams are gauge invariant, and hence the individual ingredients of the spectral method are not manifestly gauge invariant. We have therefore made considerable numerical efforts to confirm gauge invariance of the final results and thereby corroborate the enhanced spectral methods. These results show that the total fermion contribution to the energy may be negative for certain string profiles, but with magnitude that is too small to overcome the classical bosonic energy and bind the cosmic string in an $SU_L(2)$ gauge theory. However, when taking the fermion mass as about twice the top quark mass (or larger), the population of bound state levels yields a total energy that is less than the energy of equally many free fermions. Such a configuration is thus bound and can be viewed as a new solution in a model similar to the Standard Model of particle physics.

The enhanced spectral methods have furthermore enabled the first computations of the VPE of solitons with different topological charges in a renormalizable quantum field theory, for ANO vortices in the BPS version of the Abelian Higgs model with spontaneous symmetry breaking in four space—time dimensions. Here additional subtleties arise because the singular structure of the vortex cannot be removed and hampers the construction of the Born series. An alternative procedure to extract the ultra-violent divergences is needed: in particular, for the quadratic divergence that emerges from gauge-variant components that eventually cancel out in the final result. The correct (subleading) logarithmic divergence was obtained by subtracting a momentum-independent constant whose net contribution is zero but renders consistency with gauge invariance. Technically that constant is tricky to identify because it is only defined in the limit as the wave equations are solved in close vicinity of the vortex. Even after proper subtraction of that constant, the singular structure causes the angular momentum sum to converge only very slowly and an additional extrapolation is needed in numerical simulations. In the BPS case of equal gauge and scalar masses, these calculations show that the VPE is essentially proportional to a constant plus a linear function of the topological charge with negative slope. Since the classical energy is strictly linear in the charge, the vortex with a given charge has less energy than equally many vortices of unit charge and is thus stable, leading to type I behavior of superconductors in the BPS case.

Several possible extensions of these results are of interest. The restriction to the BPS case of equal masses reduces the wave equations to a two-channel problem, while in general there will be four coupled channels. Also, the case with two space dimensions differs from the calculation in three space dimensions because it does not have a complete cancellation between the contributions from the ghost fields (needed for gauge fixing) and the un-physical gauge field components. It is thus a five-channel scattering problem. In addition, the divergence structure is modified by

the lower dimensionality. Though these generalizations are tractable, their implementation is a worthwhile future project.

Acknowledgments

N.G. is supported in part by the National Science Foundation (NSF) through grant PHY-1820700. H.W. is supported in part by the National Research Foundation of South Africa (NRF) by grant 109497.

References

- 1. R. Rajaraman, Solitons and Instantons (North Holland, Amsterdam, 1982).
- 2. K. A. Milton, The Casimir Effect (World Scientific, Singapore, 2001).
- 3. D. Dalvit, P. Milonni, D. Roberts and F. da Rosa, *Casimir Physics* (Springer-Verlag, Berlin, 2011).
- 4. R. J. Perry, Nucl. Phys. A 467, 717 (1987).
- R. F. Dashen, B. Hasslacher and A. Neveu, Phys. Rev. D 10, 4114 (1974).
- 6. R. F. Dashen, B. Hasslacher and A. Neveu, Phys. Rev. D 11, 3424 (1975).
- E. Farhi, N. Graham, P. Haagensen and R. L. Jaffe, Phys. Lett. B 427, 334 (1998).
- N. Graham, M. Quandt and H. Weigel, Spectral Methods in Quantum Field Theory (Springer-Verlag, Berlin, 2009).
- 9. M. Bordag and K. Kirsten, Phys. Rev. D 53, 5753 (1996).
- F. Calegero, Variable Phase Approach to Potential Scattering (Academic Press, New York, 1967).
- N. Graham, R. L. Jaffe, V. Khemani, M. Quandt, M. Scandurra and H. Weigel, Nucl. Phys. B 645, 49 (2002).
- 12. M. Li and R. J. Perry, Phys. Rev. D 37, 1670 (1988).
- 13. B. Moussallam, Phys. Rev. D 40, 3430 (1989).
- 14. J. Baacke, Z. Phys. C 47, 263 (1990).
- 15. J. Baacke, Z. Phys. C 53, 402 (1992).
- 16. D. Ebert and H. Reinhardt, Nucl. Phys. B 271, 188 (1986).
- 17. I. G. Avramidi, Nucl. Phys. B 355, 712 (1991).
- 18. I. G. Avramidi, J. Math. Phys. 36, 5055 (1995).
- 19. J. A. Zuk, Phys. Rev. D 43, 1358 (1991).
- 20. M. Bordag, J. Phys. A 28, 755 (1995).
- 21. M. Bordag and K. Kirsten, Phys. Rev. D 60, 105019 (1999).
- 22. M. Bordag, M. Hellmund and K. Kirsten, Phys. Rev. D 61, 085008 (2000).
- 23. D. V. Vassilevich, Phys. Rept. 388, 279 (2003).
- 24. I. M. Gelfand and A. M. Yaglom, J. Math. Phys. 1, 48 (1960).
- 25. S. Coleman, Aspects of Symmetry (Cambridge University Press, 1985).
- 26. A. Parnachev and L. G. Yaffe, Phys. Rev. D 62, 105034 (2000).
- 27. G. V. Dunne and K. Kirsten, J. Phys. A 39, 11915 (2006).
- 28. G. V. Dunne and K. Kirsten, J. Phys. A 42, 075402 (2009).
- 29. J. Baacke, Phys. Rev. D 78, 065039 (2008).
- 30. G. V. Dunne, Int. J. Mod. Phys. A 27, 1260004 (2012).
- 31. H. Gies and K. Langfeld, Nucl. Phys. B 613, 353 (2001).
- 32. H. Gies and K. Langfeld, Int. J. Mod. Phys. A 17, 966 (2002).
- 33. K. Langfeld, L. Moyaerts and H. Gies, Nucl. Phys. B 646, 158 (2002).
- 34. H. Gies, K. Langfeld and L. Moyaerts, J. High Energy Phys. 06, 018 (2003).
- 35. D. Cangemi, E. D'Hoker and G. V. Dunne, Phys. Rev. D 51, 2513 (1995).

- 36. G. V. Dunne, Phys. Lett. B 467, 238 (1999).
- 37. L.-H. Chan, Phys. Rev. D 55, 6223 (1997).
- 38. I. J. R. Aitchison and C. M. Fraser, Phys. Lett. B 146, 63 (1984).
- 39. I. J. R. Aitchison and C. M. Fraser, Phys. Rev. D 31, 2605 (1985).
- 40. J. A. Bagger and S. G. Naculich, Phys. Rev. Lett. 67, 2252 (1991).
- 41. J. A. Bagger and S. G. Naculich, Phys. Rev. D 45, 1395 (1992).
- 42. J. S. Faulkner, J. Phys. C 10, 4661 (1977).
- 43. G. Barton, J. Phys. A 18, 479 (1985).
- 44. N. Graham, M. Quandt and H. Weigel, Phys. Rev. D 84, 025017 (2011).
- 45. N. Graham and H. Weigel, *Phys. Rev. D* **101**, 076006 (2020)
- N. Graham, R. L. Jaffe, M. Quandt and H. Weigel, Ann. Phys. 293, 240 (2001).
- 47. E. Farhi, N. Graham, R. L. Jaffe and H. Weigel, Nucl. Phys. B 630, 241 (2002).
- 48. G. Pöschl and E. Teller, Z. Phys. 83, 143 (1933).
- 49. H. Weigel, M. Quandt and N. Graham, Phys. Rev. D 97, 036017 (2018).
- 50. H. Weigel and N. Graham, Phys. Lett. B 783, 434 (2018).
- 51. M. A. Shifman and M. B. Voloshin, Phys. Rev. D 57, 2590 (1998).
- 52. D. Bazeia, M. J. dos Santos and R. F. Ribeiro, Phys. Lett. A 208, 84 (1995).
- 53. M. A. Lohe, Phys. Rev. D 20, 3120 (1979).
- M. A. Lohe and D. M. O'Brien, Phys. Rev. D 23, 1771 (1981).
- 55. H. Weigel, *Phys. Lett. B* **766**, 65 (2017).
- 56. A. Alonso Izquierdo and J. Mateos Guilarte, Nucl. Phys. B 852, 696 (2011).
- 57. I. Takyi, M. K. Matfunjwa and H. Weigel, Phys. Rev. D 102, 116004 (2020).
- N. Graham, M. Quandt, O. Schröder and H. Weigel, Nucl. Phys. B 758, 112 (2006).
- N. Graham, V. Khemani, M. Quandt, O. Schröder and H. Weigel, Nucl. Phys. B 707, 233 (2005).
- 60. H. Weigel, M. Quandt, N. Graham and O. Schröder, Nucl. Phys. B 831, 306 (2010).
- 61. H. Weigel and M. Quandt, Phys. Lett. B 690, 514 (2010).
- 62. M. Bordag and I. Drozdov, Phys. Rev. D 68, 065026 (2003).
- 63. F. R. Klinkhamer and C. Rupp, Nucl. Phys. B 495, 172 (1997).
- 64. H. Weigel, M. Quandt and N. Graham, Phys. Rev. D 94, 045015 (2016).
- 65. A. A. Abrikosov, Sov. Phys. JETP 5, 1174 (1957).
- 66. A. A. Abrikosov, J. Phys. Chem. Solids 2, 199 (1957).
- 67. H. B. Nielsen and P. Olesen, Nucl. Phys. B 61, 45 (1973).
- 68. B.-H. Lee and H. Min, Phys. Rev. D 51, 4458 (1995).
- 69. A. Rebhan, P. van Nieuwenhuizen and R. Wimmer, Braz. J. Phys. 34, 1273 (2004).
- 70. P. Pasipoularides, Phys. Rev. D 64, 105011 (2001).
- 71. N. Graham and H. Weigel, Phys. Rev. D 104, 011901 (2021).